Bacterial vampirism mediated through chemotaxis

Siena J. Glenn[1□], Zealon Gentry-Lear[2□], Michael Shavlik[2], Michael J. Harms[2,3], Thomas J. Asaki[4], and Arden Baylink[1*]

[1] Washington State University, Department of Veterinary Microbiology and Pathology, Pullman, WA 99164

[2] University of Oregon, Institute of Molecular Biology, Eugene, OR, 97403

[3] University of Oregon, Department of Chemistry & Biochemistry, Eugene, OR, 97403

[□] Authors contributed equally to this work.

[4] Washington State University, Department of Mathematics and Statistics, Pullman, WA 99164

[*] Corresponding author: arden.baylink@wsu.edu (A. Baylink)

Summary

Severe bacterial infections of the gastrointestinal (GI) tract instigate GI hemorrhaging that can lead to bacteremia, sepsis, and death. Pathogens preferentially colonize sites of injury, delaying healing and exacerbating tissue damage, but the underlying mechanisms are not well understood. We find that Enterobacteriaceae species are remarkably sensitive to human serum and perceive femtoliter quantities as a potent attractant. This behavior is driven by chemotaxis and the Tsr chemoreceptor, which recognizes L-serine present in serum. By studying the crystal structure of *Salmonella* Typhimurium Tsr, we identified a recognition motif for L-serine and found similar Tsr homologues in various Enterobacteriaceae species, including World Health Organization priority pathogens. Our analyses of *Escherichia* and *Citrobacter* bacteria, which also possess Tsr, confirm that these species exhibit chemoattraction to serum. We have coined the term 'vampirism' to describe this pathogenesis strategy and suggest it plays a role in injury tropism and increases the risk of bacteremia.

Introduction

Bacteria use chemosensory systems to survey and navigate their environments (Gumerov et al., 2021; Wadhwa and Berg, 2022; Zhou et al., 2022). Within the environment of the human gastrointestinal (GI) tract, chemosensing drives colonization of specific tissues based on sources

of exogenous nutrients, toxins, and molecular cues (Huang et al., 2017; Ligthart et al., 2020; Westerman et al., 2021; Zhou et al., 2022). Chemosensing directs colonization through control of motility and adhesion systems such as chemotaxis, chemokinesis, twitching, and biofilm formation (Jakuszeit et al., 2021; Kearns, 2010; Perkins et al., 2021; Zhou et al., 2022). Most bacterial genera identified by the World Health Organization (WHO) as 'priority pathogens' employ sophisticated chemosensory systems for efficient infection and exert precise control over their colonization topography (Murray et al., 2022; Tacconelli et al., 2018; Zhou et al., 2022). These include multidrug-resistant Enterobacteriaceae pathogens of the gut such as *Salmonella enterica*, Enterohemorrhagic *Escherichia coli* (EHEC), *Citrobacter koseri*, and *Enterobacter cloacae*, which present major challenges for global health (Tacconelli et al., 2018; Zhou et al., 2022). Mapping the physicochemical signals pathogens use to direct colonization will improve understanding of how chemosensing contributes to pathogenesis and clinical outcomes (Donaldson et al., 2016; Zhou et al., 2022).

Sepsis is the leading cause of death for those with inflammatory bowel diseases (IBD), such as Crohn's Disease (31.1%) and Ulcerative Colitis (43.4%) (Weber et al., 2020), driven primarily by systemic Enterobacteriaceae infections (Goren et al., 2020). Intestinal intra-abdominal abscesses, microperforations, and fistulas associated with IBD predispose patients to GI bleeding and bacteremia (Satoh et al., n.d.; Vohra et al., 2020). More broadly, GI bleeding is associated with significant risk of mortality, in the range of 6-30%, and impacts 40-150 of every 100,000 individuals annually (Fig. 1) (Aljarad and Mobayed, 2021; Huang et al., 2021; Kim et al., 2014, 2014; Moledina and Komba, 2017; Saltzman, 2022; Scales and Huffnagle, 2013; Tacconelli et al., 2018; Zhou et al., 2022). GI pathogens demonstrate specific affinity for inflamed and damaged tissue (Fig. 1) (Aihara et al., 2014; Callahan et al., n.d.; Croxen and Finlay, 2010; Hanyu et al., 2019; Rivera-Chávez et al., 2013a; Scales and Huffnagle, 2013; Zhou et al., 2022). Accumulation of bacteria at lesions exacerbates tissue damage, delays wound healing, and increases risk of systemic infection (Hanyu et al., 2019; Minasyan, 2019). The mechanisms by which bacteria target sites of inflammation and injury, and the physiological benefits of injury tropism for bacteria, remain poorly understood.

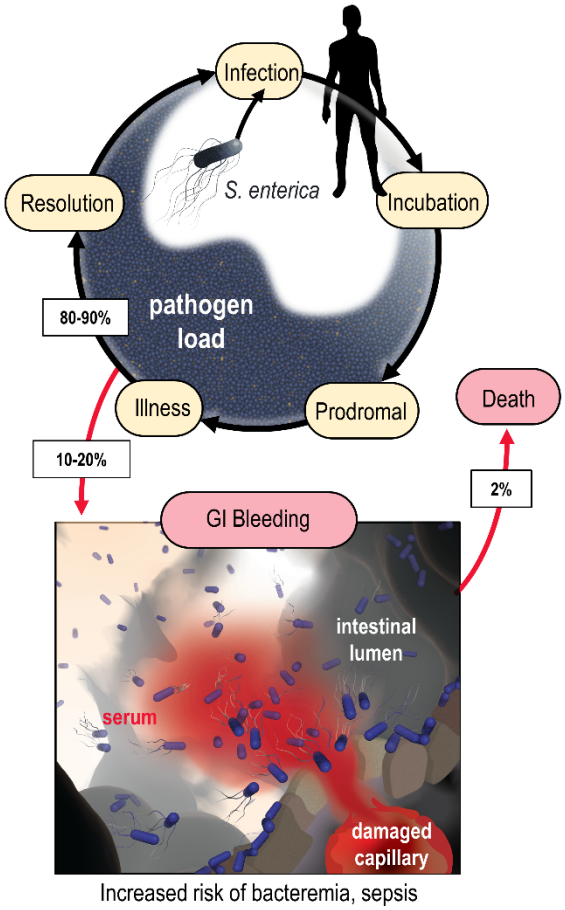

Fig. 1. Model of the microenvironment of bacterial-induced hemorrhagic lesions. The typical course of non-typhoidal *S. enterica* infections is shown proceeding through infection, incubation, prodromal, illness, and resolution stages (black arrows). The atypical route of GI bleeding, associated with increased mortality and morbidity, is shown in red arrows, with rates approximated from available literature. An artistic depiction of bacterial injury tropism is shown bottom.

To address this open question, we investigated whether GI bleeding could be perceived by pathogen chemosensing systems, and what effect, if any, this has on bacterial localization. Blood, and its liquid component, serum, contains sugars and amino acids in the millimolar range—on the order of 1,000,000-fold greater than other sources available to gut microbes—as well as iron, zinc, and other metals that serve as valuable nutrients for bacteria and enhance their virulence (Murdoch and Skaar, 2022; Zhou et al., 2022). Serum also contains antibacterial factors that hinder bacterial survival in the bloodstream through complement-mediated killing, so it was unclear how enteric pathogens would respond to exposure to serum (Cheng et al., 2019).

Studying these behaviors *in vivo* poses challenges due to the rapidity of bacterial chemosensory responses and the species-specific hemodynamic, immunogenic, pharmacokinetic, and chemical properties of blood and serum (Mestas and Hughes, 2004; Namdee et al., 2015; Zhao et al., 2020). For instance, human blood glucose levels (5.6-6.9 mM) are higher than mice (4.3 mM) (Munekawa et al., 2022; Paul et al., 2011).

To circumvent these challenges, we developed a specialized *in vitro* live-imaging system to simulate GI bleeding using human serum and observe bacterial responses in real-time. We first investigated non-typhoidal serovars of the human enteric pathogen *S. enterica* as exemplars of Enterobacteriaceae that can cause GI hemorrhaging and sepsis (Fig. 1). These serovars are responsible for approximately 1.35 million infections each year and possess chemosensory systems characteristic of Enterobacteriaceae (Medicine, 2020; Zhou et al., 2022). Our investigation reveals that *S. enterica* exhibits a remarkable sensitivity to human serum, is attracted to it, and utilizes serum nutrients to gain a growth advantage. We introduce the term "vampirism" to describe this pathogenesis strategy. Furthermore, we confirmed the presence of this mechanism in the Enterobacteriaceae species *E. coli* and *C. koseri*, indicating that bacterial vampirism is a widespread behavior that may contribute to increased risk of bacteremia and sepsis.

Results

Use of the chemosensory injection rig assay (CIRA) to model biological microgradients

The microenvironment of an enteric hemorrhagic lesion involves a source of whole blood emanating from the host tissue and diffusing into the intestinal lumen (Fig. 1). In effect, this creates a microscopic gradient, i.e., a microgradient, of chemicals flowing outward from a point source that may serve as chemosensory signals for luminal bacteria. To model features of enteric bleeding *in vitro*, we designed an experimental system to inject minute quantities of human serum into a pond of motile bacteria and observe real-time responses by microscopy (Fig. 2A). Our system and methodology, which we refer to herein as the chemosensory injection rig assay (CIRA), offers several advantages for modeling bacterial localization in response to enteric bleeding: (1) we can use bona fide human serum, (2) the readouts are direct measurements of real-time localization dynamics of the bacterial population, and (3) similar to a bleeding event, a source of fresh serum continuously flows outward. By employing multichannel fluorescence

imaging of differentially labeled bacterial populations we observe a head-to-head comparison of bacterial behavior within the same experiment.

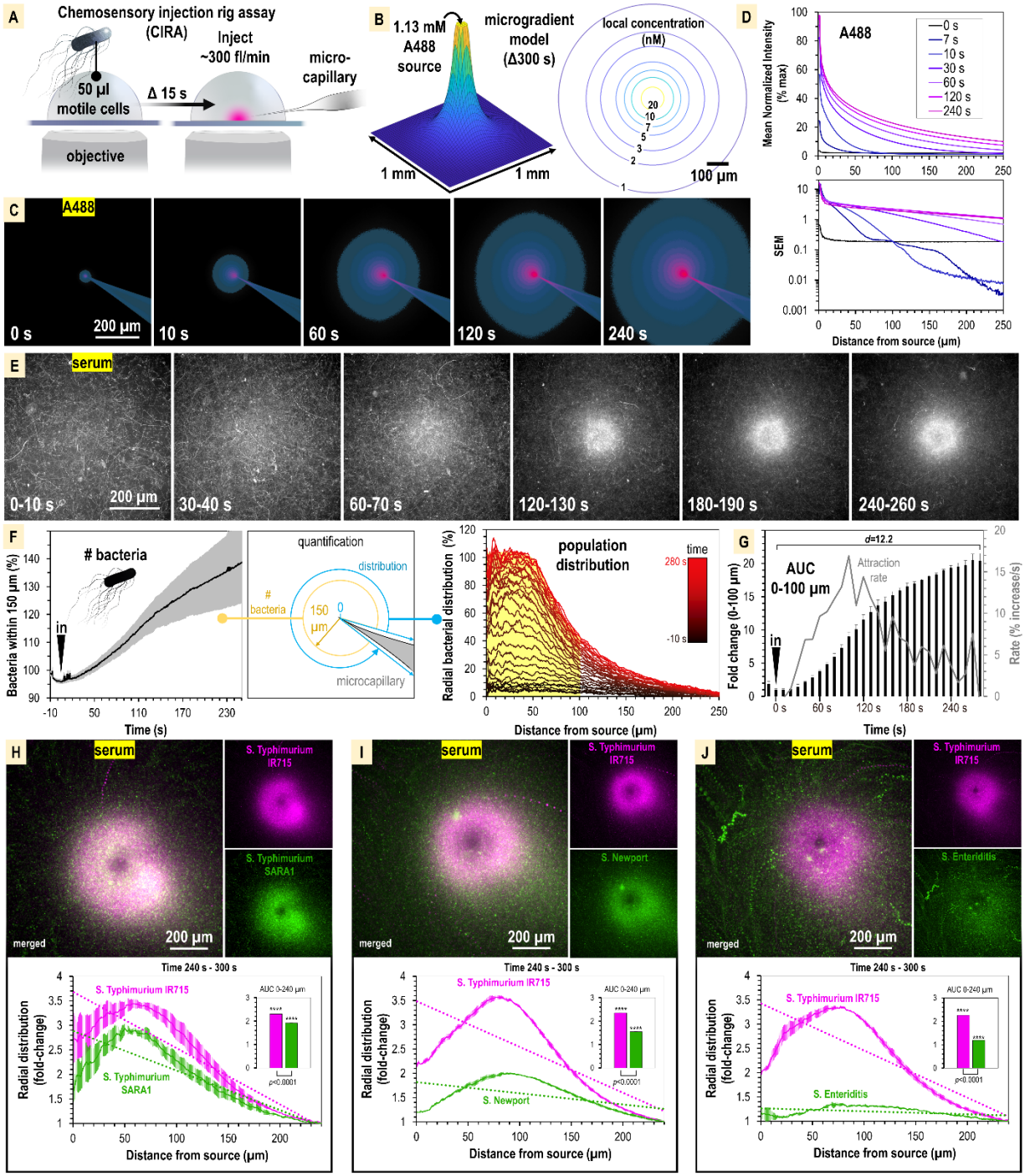

Fig. 2. *S. enterica* serovars rapidly localize toward human serum. A. CIRA experimental design. B. CIRA microgradient model, simulated with a source of 1.13 mM A488 dye after 300 s of injection. C. Visualization of the CIRA microgradient with A488 dye. D. Radial distribution of A488 dye at representative time points (n=6). E. Response of *S. enterica* Typhimurium IR715 to human serum (max projections over 10 s intervals). F. Quantification of *S. enterica* Typhimurium IR715 attraction response to human serum (n=4, 37˚ C) characterized as either the relative number of bacteria within 150 µM of the source (left), or the radial distribution of the bacterial population over time (right, shown in 10 s intervals). G. Area under the curve (AUC) versus time for the bacterial population within 100 µm of the serum treatment source (area indicated in yellow in panel F). Effect size (Cohen's *d*) between the treatment start and endpoints is indicated. Insertion of the treatment microcapillary is indicated with black arrow. Attraction rate over time indicated in gray. H-J. CIRA competition experiments between *S.* Typhimurium IR715 (pink) and clinical isolates (green) responding to human serum for 5 mins (n=4, 37˚ C). Images are representative max projections over the final minute of treatment. Radial distributions calculated from max projections and averaged across replicates are shown as fold-change relative to the image periphery at 240 µm from the source. Inset plots show fold-change AUC of strains in the same experiment, with *p*-values from unpaired two-sided t-test, or one-sided t-test (stars) relative to an expected baseline of 1. Trend lines (dashed) indicate the degree of bias in the population distribution, with increasingly negative slope reflecting greater chemoattraction. Data shown are means, error bars indicate SEM. See also Fig. S1, Key Resources Table, Movie S1, Movie S2.

The CIRA microgradient is established through injection at a constant rate of ~300 femtoliters per minute, through a 0.5 µm glass microcapillary, and expands over time from diffusion (Fig. 2A-B, Fig. S1). To approximate the diffusion of serum metabolites we developed a mathematical model for the CIRA microgradient based on the three-dimensional differential diffusion equation (Fig. 2B, Fig. S1, Method Details). From this model, we calculate that the introduction of a minute volume of novel effector produces a steep microgradient, in which a millimolar source recedes to nanomolar concentrations after diffusion across only a few hundred microns (Fig. 2B, Fig. S1). For instance, we expect a bacterium 100 µm from a 1 mM infinite source to experience a local concentration of a small molecule effector (diffusion coefficient approximately 4×10^{-6} cm^2 s^{-1}) of 10 nM after 300 s of injection (Fig. 2B, Fig. S1). To visualize the microgradient experimentally, we utilized Alexa Fluor 488 dye (A488) and observed the microgradient to be stable and consistent across replicates (Fig. 2C-D, Movie S1). We found no behavioral differences in treatments with buffer in the range of pH 4-9, indicating small, localized pH changes are inconsequential for taxis in our system, and that any artifactual forces, such as flow, account for only minor changes to bacterial distribution at the population level, in the range of ±10% (Fig. S1).

S. enterica exhibits rapid attraction to human serum

We first studied the chemosensing behaviors of *S.* Typhimurium IR715, which is a derivative of ATCC 14028, originally isolated from domesticated chickens, and is used extensively in the study of *Salmonella* pathogenesis (Key Resources Table)(Rivera-Chávez et al., 2016, 2013b; Tsolis et al., 1999; Winter et al., 2010). As treatment, we utilized active human serum, i.e. serum that was not heat-inactivated nor exposed to chemical or physical treatments that would alter its native complement properties (see Method Details). We assessed the response of motile IR715, containing a fluorescent mPlum marker, to a source of human serum over the course of 5 minutes (Fig. 2E, Movie S1). During this timeframe, we witnessed a rapid attraction response whereby the motile bacterial population reorganized from a random distribution to one concentrated within a 100-150 µm radius of the serum source (Fig. 2E-F, Movie S1). To compare responses between CIRA experiments, we plotted data as either the relative number of bacteria within 150 µm of the treatment (Fig. 2F, left panel) or a radial distribution of the population (Fig. 2F, right panel) over time. By these measures we determined *S.* Typhimurium IR715 is attracted to human serum. The bacterial population in proximity to the serum source doubles by 40 s, reaches a maximal attraction rate by 90 s, and approaches equilibrium by 300 s post-treatment (Fig. 2G).

To test whether serum attraction is relevant for *Salmonella* strains that infect humans, and if responses differ among non-typhoidal *Salmonella* serovars, we employed dual-channel CIRA imaging to compete *S.* Typhimurium IR715 against representative clinical isolates of Typhimurium (SARA1), Newport (M11018046001A), and Enteriditis (05E01375). These serovars are the most common in North American infections (Ferrari et al., 2019). All strains showed attraction responses to human serum, seen as a significant distribution bias toward the serum source relative to the experiment periphery (Fig. 2H-J, Movie S2). The magnitude of the attraction response was weaker for *S.* Newport and *S.* Enteriditis than for *S.* Typhimurium (Fig. 2H-J, Movie S2). Together, our data show *S. enterica* serovars that cause disease in humans are exquisitely sensitive to human serum, responding to femtoliter quantities as an attractant, and that distinct reorganization at the population level occurs within minutes of exposure (Fig. 2H-J, Movie S2).

Chemotaxis and the chemoreceptor Tsr mediate serum attraction

Serum is a complex biological solution containing a variety of sugars, amino acids, and other metabolites that could serve as attractant signals (Zhou et al., 2022). Based on the rapid accumulation of bacteria toward the treatment source, characteristic of chemotactic behaviors (Huang et al., 2015), we hypothesized serum to be perceived through the chemotaxis system, and that one or more of these chemical components could be specifically recognized as chemoattractants through the repertoire of chemoreceptors possessed by *Salmonellae* (Fig. 3A). Based on current understanding of chemoreceptor-chemoattractant ligand interactions (Matilla et al., 2022; Zhou et al., 2022), we identified three chemoreceptors that could mediate serum chemoattraction: (1) taxis to serine and repellents (Tsr), which responds to L-serine, and reportedly also norepinephrine (NE) and 3,4-dihydroxymandelic acid (DHMA); (2) taxis to ribose and glucose/galactose (Trg), which responds to glucose and galactose; and (3) taxis to aspartate and repellents (Tar), which responds to L-aspartate (Fig. 3A). We modeled the local concentration profile of these effectors based on their typical concentrations in human serum (Fig. 3B). The two most prevalent chemoattractants in serum are glucose (5 mM) and L-serine (100-300 µM) (Fig. 3B-F), which suggest the chemoreceptors Trg and/or Tsr could mediate serum attraction. These chemoreceptors were shown previously to be important for infection and survival in the inflamed gut, with complemented strains rescuing the colonization defect of chemoreceptor deletion mutants (Rivera-Chávez et al., 2013b).

To test the role of chemotaxis in serum attraction, we competed wildtype (WT) *S.* Typhimurium IR715 against a chemotaxis-null isogenic *cheY* mutant, which is motile but blind to chemoeffector signals (Fig. 3G, Movie S3). Whereas the WT mounts a robust attraction response to serum, the *cheY* mutant population remains randomly distributed (Fig. 3G, Movie S3). We also observed the *cheY* mutant to exhibit a slight decline in cells proximal to the treatment source over time, which we attribute to cellular crowding effects from the influx of WT cells (Fig. 3G, Movie S3). In this background, the fraction of WT cells within 100 µm of the serum source increases by 70-fold, with maximal rate of attraction achieved by 120 s post treatment. Thus, we determined that chemotaxis, i.e., chemoattraction, is namely responsible for the rapid localization of *S. enterica* to human serum, and other mechanisms of localization control, such as chemokinesis and type IV pili-mediated motility, are inconsequential under these conditions.

We next analyzed strains with deletions of the chemoreceptors *trg*, or *tsr*, to test the roles of these chemoreceptors in mediating serum chemoattraction. Surprisingly, we found the *trg* strain to be non-motile (data not shown). Because motility is a prerequisite for chemotaxis, we chose not to study the *trg* mutant further, and instead focused our mechanistic investigations on Tsr. We compared chemoattraction responses in dual-channel CIRA experiments between the WT and *tsr* mutant and observed an interesting behavior whereby both strains exhibited chemoattraction, but the *tsr* mutant distribution was relegated to a halo at the periphery of the WT peak (Fig. 3H, Movie S3). The WT efficiently outcompetes the *tsr* mutant such that by 5 minutes post-treatment the ratio of WT to *tsr* cells proximal to the serum source is 3:1 (Fig. 3H, Movie S3). Similar to *cheY*, we presume the *tsr* halo results from cellular crowding effects induced by the high density of WT cells near the serum source. To test how the *tsr* mutant responds to serum in the absence of a strong competitor, we compared chemoattraction between *tsr* and *cheY*. In this background, *tsr* chemoattraction remained diminished relative to that of WT, but the *tsr* distribution shifted closer to the serum source (Fig. 3I, Movie S3). These results lead us to conclude that the mechanism underlying serum chemoattraction involves the chemoreceptor Tsr and acts through one, or more, of the chemoattractants recognized by Tsr that is present in serum: L-serine, NE, or DHMA.

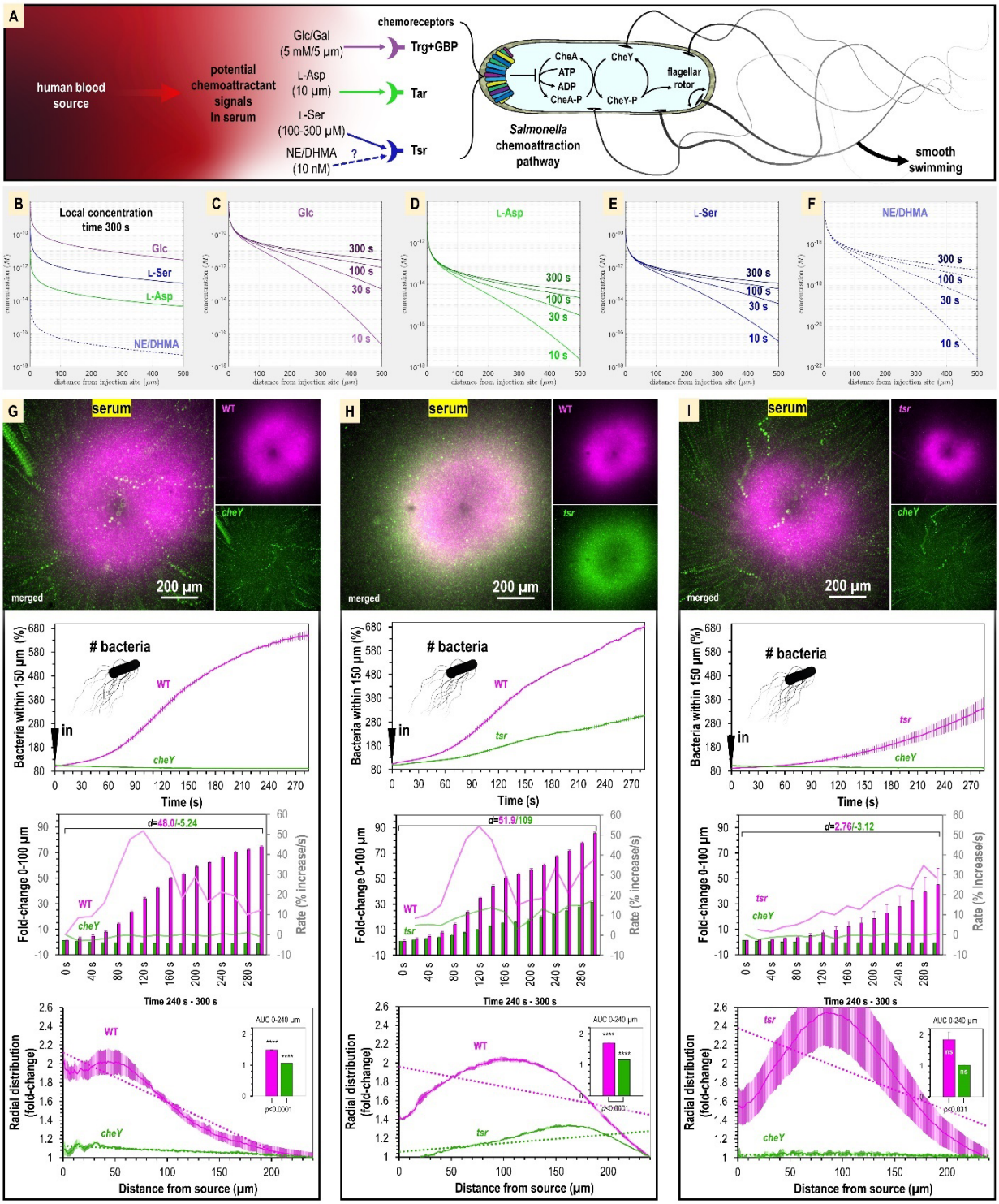
A
human blood source
potential chemoattractant signals in serum
Glc/Gal (5 mM/5 µM)
L-Asp (10 µM)
L-Ser (100-300 µM)
NE/DHMA (10 nM)
chemoreceptors
Trg+GBP
Tar
Tsr
CheA
CheY
ATP
ADP
CheA-P
CheY-P
flagellar rotor
Salmonella chemoattraction pathway
smooth swimming
B
Local concentration time 300 s
Glc
L-Ser
L-Asp
NE/DHMA
C
Glc
D
L-Asp
E
L-Ser
F
NE/DHMA
300 s
100 s
30 s
10 s
distance from injection site (µm)
G
serum
WT
cheY
merged
200 µm
H
serum
WT
tsr
merged
200 µm
I
serum
tsr
cheY
merged
200 µm
bacteria
in
Bacteria within 150 µm (%)
Time (s)
d=48.0/-5.24
d=51.9/109
d=2.76/-3.12
Fold-change 0-100 µm
Rate (% increase/s)
Time 240 s - 300 s
AUC 0-240 µm
p<0.0001
p<0.031
ns
Radial distribution (fold-change)
Distance from source (µm)

223

Fig. 3. Attraction to human serum is mediated through chemotaxis and the chemoreceptor Tsr. A. Potential mechanisms involved in *Salmonella* sensing of chemoattractants present in human serum. Approximate concentrations of these effectors in human serum are indicated in parentheses (Zhou et al., 2022). B-F. Microgradient modeling of serum chemoattractant concentrations. G-H. CIRA competition experiments between *S.* Typhimurium IR715 WT and isogenic mutants *cheY*, or *tsr*, and *tsr* versus *cheY*, in response to human serum (n=3-4, 37˚ C). Rates in terms of fold-change are indicated with light pink/light green lines and plotted on the gray secondary y-axis. Data are means and error bars are SEM. See also Key Resources Table, Movie S3.

S. enterica exhibits chemoattraction to L-serine, but not NE or DHMA

To identify the specific chemoattractants driving Tsr-mediated serum chemoattraction, we used CIRA to examine responses to purified effectors diluted in buffer. The concentration of L-serine in human serum ranges from approximately 100-400 µm, depending on diet and health factors (He et al., 2022; Miller et al., 2020; Pitkänen et al., 2003), whereas the neurotransmitters NE, and its metabolized form, DHMA, are thought to circulate at 10,000-fold lower concentrations, approximately 10 nM (Kopin et al., 1978; Steuer et al., 2016). Nevertheless, it has been proposed that NE and/or DHMA are sensed directly by Tsr with nanomolar affinity (Orr et al., 2020; Pasupuleti et al., 2014).

We used CIRA to test the response of *S. Typhimurium* IR715 to L-serine, NE, and DHMA. We observed robust chemoattraction responses to L-serine, but no detectable response to either NE or DHMA (Fig. S2, Movie S4-6). We attempted additional CIRA experiments with cells cultured according to prior work, which included 'priming' the cells with NE before chemotaxis experiments, but ultimately saw no evidence to suggest *S. enterica* responds chemotactically to NE or DHMA (Fig. S2, Movie S5-6). This indicates the chemoattractant in serum sensed through Tsr is L-serine.

Chemoattraction to L-serine has mostly been studied in the context of model laboratory strains, like IR715, and has not been rigorously evaluated for *S. enterica* clinical isolates or various serovars. To establish whether L-serine sensing is relevant for human infections, we used dual-channel CIRA to compare taxis to L-serine between IR715 and clinical isolates (Fig. 4A-C, Movie S4). In each case we observe robust chemoattraction, though there are differences in sensitivity to L-serine. The magnitude of chemoattraction was highest for *S.* Typhimurium SARA1 and *S.* Newport, whereas *S.* Typhimurium IR715 and *S.* Enteriditis showed lower

responses, which could relate to the different host specificities of these serovars and strains (Fig. 4A-C, Movie S4).

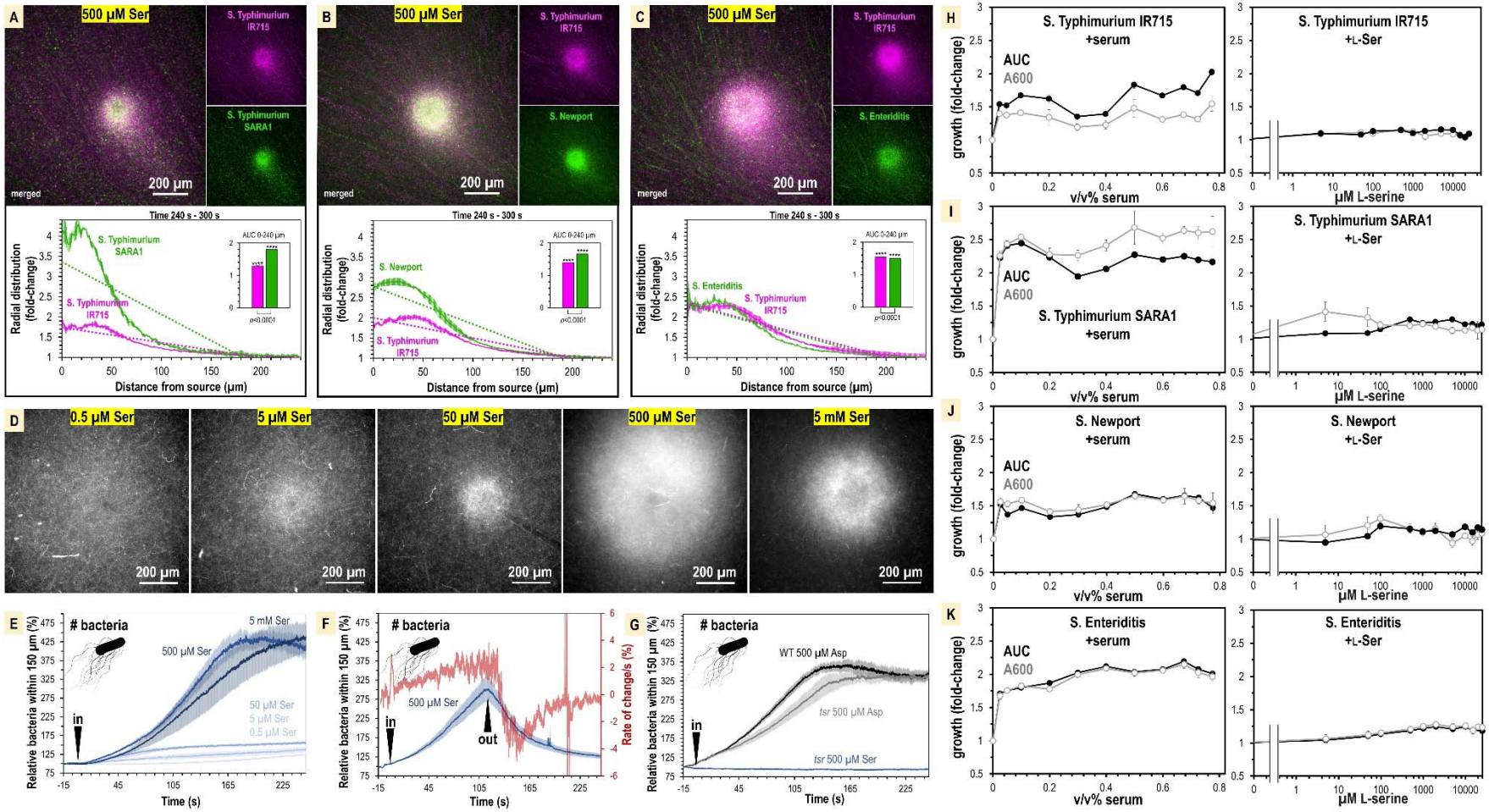
A
500 µM Ser
S. Typhimurium IR715
S. Typhimurium SARA1
merged
200 µm
B
500 µM Ser
S. Typhimurium IR715
S. Newport
merged
200 µm
C
500 µM Ser
S. Typhimurium IR715
S. Enteriditis
merged
200 µm
Time 240 s - 300 s
Radial distribution (fold-change)
Distance from source (µm)
AUC 0-240 µm
D
0.5 µM Ser
5 µM Ser
50 µM Ser
500 µM Ser
5 mM Ser
200 µm
E
bacteria
5 mM Ser
500 µM Ser
50 µM Ser
5 µM Ser
0.5 µM Ser
in
Relative bacteria within 150 µm (%)
Time (s)
F
bacteria
500 µM Ser
in
out
Rate of change/s (%)
G
bacteria
WT 500 µM Asp
tsr 500 µM Asp
tsr 500 µM Ser
H
S. Typhimurium IR715
+serum
AUC
A600
growth (fold-change)
v/v% serum
S. Typhimurium IR715
+L-Ser
µM L-serine
I
S. Typhimurium SARA1
+serum
S. Typhimurium SARA1
+L-Ser
J
S. Newport
+serum
S. Newport
+L-Ser
K
S. Enteriditis
+serum
S. Enteriditis
+L-Ser

257

Fig. 4. L-serine is sensed as a chemoattractant molecular cue but provides little growth advantage. A-C. CIRA competition experiments between *S.* Typhimurium IR715 (pink) and clinical isolates (green) in response to 500 µM L-serine (n=3, 37˚ C). D. Representative results showing max projections of *S.* Typhimurium IR715 at 240 – 300 s post CIRA treatment with L-serine concentrations (30˚ C). E. Quantification of multiple replicate experiments shown in D. F. Attraction and dispersion of *S.* Typhimurium IR715 following addition and removal of 500 µM L-serine source (30˚ C). G. *S.* Typhimurium IR715 WT or *tsr* mutant responses to L-aspartate or L-serine treatments (30˚ C). H-I. Serum provides a growth benefit for diverse *S. enterica* serovars, that is not recapitulated by L-serine treatment alone. Growth is shown as area under the curve (AUC, black) and A600 at mid-log phase for the untreated replicates (gray, n=16). Data are means and error is SEM. See also Fig. S2, Fig. S3, Fig. S4, Movie S4, Movie S5, Movie S6.

We next used CIRA to test a range of L-serine sources spanning five orders of magnitude to define whether the concentrations of L-serine present in human serum are sufficient to drive a chemoattraction response. Within the 5 min timeframe of our experiments, the minimal source concentration of L-serine inducing chemoattraction is 0.5-5 µM. The [L-serine] required for half maximal chemoattraction (i.e., $K_{1/2}$) is approximately 105 µM (Fig. 4D-E, Fig. S3). Based on our microgradient modeling, this corresponds to a local L-serine concentration of 4.35 nM for bacteria 100 µm from the source (Fig. S1, Fig. 3B). To gain further insights into the dynamics of L-serine chemoattraction, we monitored chemotactic behavior in the presence of L-serine, and then removed the treatment (Fig. 4F). These experiments showed maximal attraction and dispersal rates to be similar, changing by approximately 4% per second (Fig. 4F). These findings emphasize the rapid dynamics through which chemotaxis can influence the localization of bacteria in response to microscopic gradients of chemoeffectors.

To substantiate our findings, we considered some alternative explanations for our data. First, we tested whether Tsr alone was required for chemoattraction to L-serine, or whether some other chemoreceptor, or form of taxis, such as energy or redox taxis, might contribute to the responses. However, we found when treated with L-serine, the *tsr* mutant showed no chemoattraction and behaved similarly to the chemotaxis-null *cheY* mutant (Fig. 4G). Second, we considered the possibility that the defect in serum chemoattraction of the *tsr* mutant could be due to pleiotropic effects of the *tsr* deletion on chemotaxis signaling or motility, similar to the inhibited swimming motility of the *trg* mutant. We tested the ability of the *tsr* strain to respond to another chemoattractant, L-aspartate, which is sensed through the Tar chemoreceptor (Fig. 3A).

We found that the *tsr* mutant mounted a robust chemoattraction response to 500 µM L-aspartate, similar in magnitude and rate to WT (Fig. 4G), supporting that chemotaxis to non-serine stimuli remains functional in the *tsr* strain. Together, these data support that the mechanism of Tsr-mediated chemoattraction to serum is through direct recognition of L-serine.

Serum provides a growth advantage for non-typhoidal S. enterica serovars

The robust serum chemoattraction response conserved across diverse *Salmonella* serovars suggests serum, and L-serine present in serum, could be a source of nutrients during infection. Yet, serum also contains complement proteins and bactericidal factors, such as defensins and cathelicidin, that could inhibit bacterial growth (Cheng et al., 2019). To address this, we investigated whether active human serum provides a growth benefit for *Salmonella* in a background of minimal media. In all strains surveyed, we found that serum addition enhances growth, and we saw no evidence of killing even for the highest serum concentrations tested (Fig. 4H-K). The growth enhancement required relatively little serum, as 2.5% v/v was sufficient to provide a 1.5-2.5-fold growth increase (Fig. 4H-K).

Since L-serine is not only a chemoattractant, but also an important nutrient for bacteria in the gut (Zhou et al., 2022), we hypothesized the growth benefit could be from L-serine. We determined by mass spectrometry that our human serum samples contain 241 µM +/- 48 total serine (L- and D-enantiomers), of which approximately 99% is expected to be L-serine (Hashimoto et al., 2003) (Fig. S4). We attempted to treat human serum with a purified recombinant enzyme that degrades L-serine, serine dehydrogenase (SDS), to see whether serine-depleted serum would elicit less growth or chemoattraction. However, these treatments did not alter serum serine content relative to untreated samples, and so we abandoned this approach (Fig. S4). Instead, we performed a titration of purified L-serine and assessed its role in supporting a growth advantage. We found that only a very small benefit is achieved with the addition of L-serine, which did not recapitulate the larger growth benefit seen for serum addition (Fig. 4H-K). This leads us to believe that L-serine functions as a molecular cue that directs *Salmonella* toward serum, but nutrients present in serum other than L-serine provide the growth advantages.

Structure of S. enterica Tsr in complex with L-serine

We next undertook structural studies to understand the specific recognition of L-serine by Tsr. The full-length Tsr protein includes a periplasmic ligand-binding domain (LBD), a transmembrane HAMP domain, and a cytosolic coiled-coil region, which oligomerizes to form trimers-of-dimers, and complexes with the downstream chemotaxis signaling components, CheA and CheW (Fig. 5A) (Cassidy et al., 2020). No experimentally-determined structure has been published for *S. enterica* Tsr (*Se*Tsr) and the single experimentally-determined structure to have captured the L-serine-binding interactions is a crystal structure of *Ec*Tsr LBD of moderate resolution (2.5 Å, PDB: 3atp) where the electron density for the ligand is weak and the orientation of the L-serine ligand is ambiguous (Tajima et al., 2011). We recognized that in the prior *Ec*Tsr study, the methods described exchanging the protein crystal into a glycerol cryoprotectant. We hypothesized the serine ligand leached out of the crystal, leaving the binding site partially occupied, and caused the electron density to be weak for the ligand and binding region. To capture a complex with a fully-bound ligand site we grew crystals of the soluble periplasmic portion of the *Se*Tsr LBD with L-serine, at a high salt concentration that would serve as a cryoprotectant without further manipulation, and harvested crystals directly from drops so as to prevent leaching of the ligand from the binding site. We identified a single *Se*Tsr LBD crystal that diffracted to high resolution (2.2 Å) and was of sufficient quality for structure determination (Fig. 5B, Table S1).

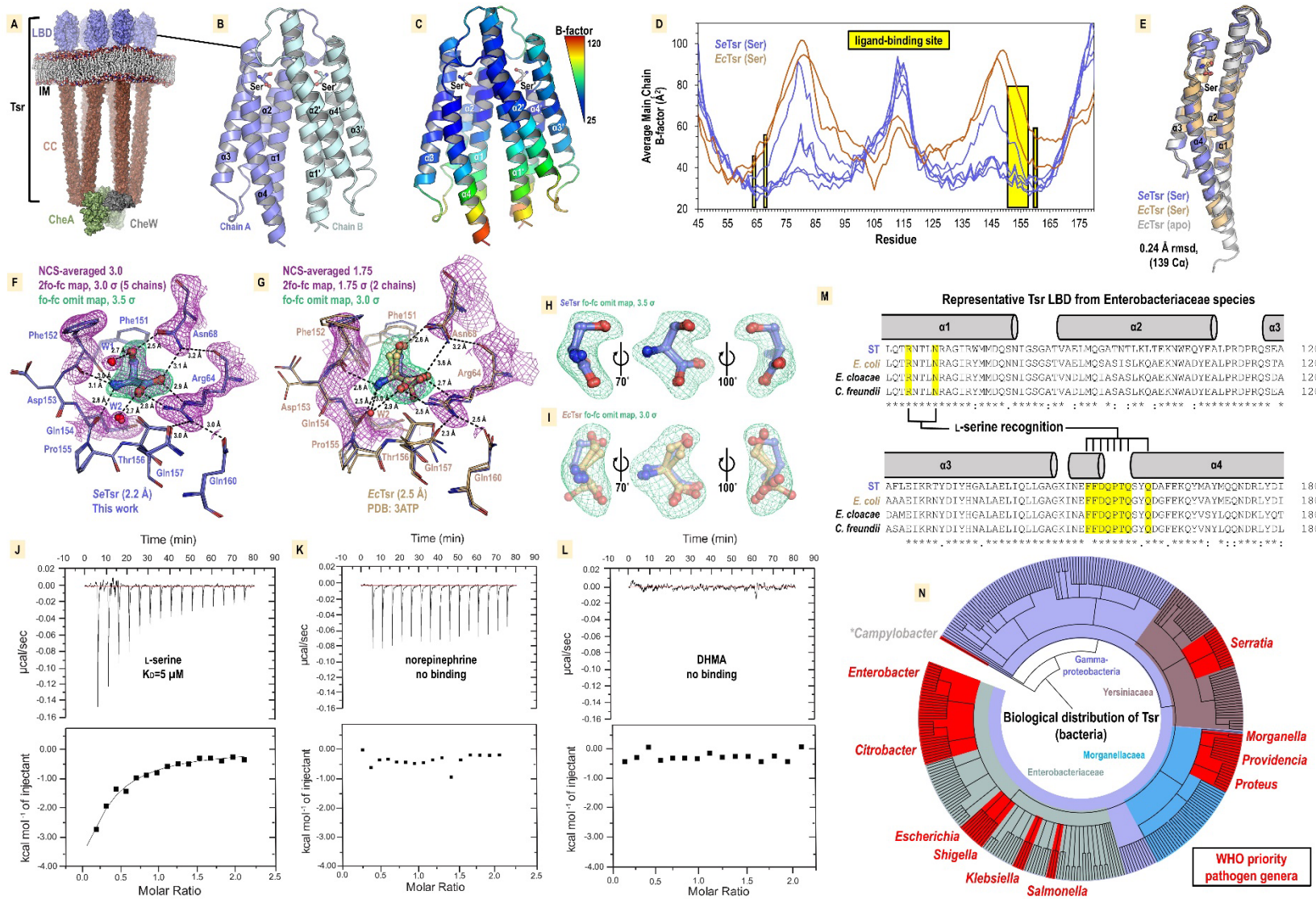
A
LBD
IM
Tsr
CC
CheA
CheW
B
Chain A
Chain B
C
B-factor
120
25
D
ligand-binding site
SeTsr (Ser)
EcTsr (Ser)
Average Main Chain B-factor (Å²)
Residue
E
SeTsr (Ser)
EcTsr (Ser)
EcTsr (apo)
0.24 Å rmsd, (139 Cα)
F
NCS-averaged 3.0
2fo-fc map, 3.0 σ (5 chains)
fo-fc omit map, 3.5 σ
SeTsr (2.2 Å)
This work
G
NCS-averaged 1.75
2fo-fc map, 1.75 σ (2 chains)
fo-fc omit map, 3.0 σ
EcTsr (2.5 Å)
PDB: 3ATP
H
SeTsr fo-fc omit map, 3.5 σ
I
EcTsr fo-fc omit map, 3.0 σ
M
Representative Tsr LBD from Enterobacteriaceae species
L-serine recognition
N
Biological distribution of Tsr (bacteria)
Campylobacter
Enterobacter
Citrobacter
Escherichia
Shigella
Klebsiella
Salmonella
Serratia
Morganella
Providencia
Proteus
Gamma-proteobacteria
Yersiniaceae
Morganellaceae
Enterobacteriaceae
WHO priority pathogen genera
J
L-serine
KD=5 μM
K
norepinephrine
no binding
L
DHMA
no binding
Time (min)
μcal/sec
kcal mol⁻¹ of injectant
Molar Ratio

Fig. 5. Structural mechanism underlying L-serine chemoattraction. A. Model of the core chemoreceptor signaling unit showing two full-length Tsr chemoreceptor trimer-of-dimers; coiled-coil region (CC), inner membrane (IM) (Cassidy et al., 2020). B. Crystal structure of *S. enterica* Tsr LBD dimer in complex with L-serine (2.2 Å). C-D. Relative order of the *Se*Tsr dimer as indicated by B-factor ($Å^2$). E. Overlay of chains from serine-bound *Se*Tsr (blue), serine-bound *Ec*Tsr (orange), and apo *Ec*Tsr (white). F. Binding of the L-serine ligand as seen with an overlay of the 5 unique chains of the asymmetric unit (AU) in the *Se*Tsr structure. Purple mesh represents non-crystallographic symmetry $2f_o$-f_c omit map electron density (ligand not included in the density calculations). Green mesh represents f_o-f_c omit map difference density for Chain A. Hydrogen bonds to the ligand are shown as dashed black lines with distances indicated in Angstroms (Å). G. The ligand-binding site of serine-bound *Ec*Tsr is shown as in F, with omit map f_o-f_c electron density. The two chains of *Ec*Tsr in the AU are overlaid (orange) with one chain of serine-bound *Se*Tsr (blue). H-I. Closeup view of the L-serine ligand and f_o-f_c omit map density for the *Se*Tsr (blue) and *Ec*Tsr (orange) structures, respectively. J-L. Isothermal titration calorimetry analyses of the *Se*Tsr LBD with L-serine, NE, or DHMA. M. Sequence conservation among Enterobacteriaceae with residues of the L-serine ligand-binding pocket highlighted. N. Biological distribution of Tsr homologues. See also Move S7, Data S1, and Table S1.

The crystal structure of *Se*Tsr LBD contains five monomers in the asymmetric unit, providing five independent views of the L-serine binding site, with homodimers formed between Chains A and B, C and D, and E and its crystal symmetry mate, E′ (Fig. 5B). Lower B-factors in the *Se*Tsr ligand binding region are indicative of greater order, reflecting that our structure is fully serine-bound (Fig. 5C-D). *Se*Tsr and *Ec*Tsr possess high sequence similarity in the LBD region (82.1% identity), and as expected, retain a similar global structure with all chains of serine-bound *Se*Tsr (5), serine-bound *Ec*Tsr (2), and apo *Ec*Tsr (2) overlaying within 0.24 Å rmsd over 139 C_α (Fig. 5E).

Molecular recognition of L-serine by SeTsr

The higher resolution (+0.3 Å) of the *Se*Tsr structure, and full occupancy of the ligand, provide a much-improved view of the interactions that facilitate specific recognition of L-serine (Fig. 5F-G). Using non-crystallographic symmetry averaging, we leveraged the five independent *Se*Tsr monomers to generate a well-defined $2f_o$-f_c map of the L-serine ligand and residues involved in ligand coordination (Fig. 5F, Movie S7). Omit-map difference density, which is calculated in the absence of a modeled ligand and reduces potential bias in the electron density map, was fit well by the placement of the L-serine ligand (Fig. 5F). In this orientation, the ligand is in an optimal energetic conformation that satisfies all possible hydrogen bonding interactions: the positively-

charged peptide amine donates hydrogen bonds to the backbone carbonyl oxygens of Phe151, Phe152, and Gln154, the negatively-charged ligand carboxyl group donates hydrogen bonds to the Arg64 guanidinium group, the Asn68 side change amine, and a water (W2), and the ligand hydroxyl sidechain donates a hydrogen bond to the Asn68 sidechain oxygen, and accepts a hydrogen bond from a water (W1) (Fig. 5F, Movie S7). All five chains of the *Se*Tsr structure are consistent in the positions of the ligand and surrounding residues (Fig. 5F, Movie S7).

With the aid of the improved view provided by our *Se*Tsr structure, we noticed the L-serine to be positioned differently than modeled in the *Ec*Tsr structure (Fig. 5F-G, Movie S7). The *Ec*Tsr serine is modeled with the sidechain hydroxyl facing into the pocket toward Asn68, and the orientations of Asn68, Phe152, Asp153, and Gln157 ligand binding pocket are modeled inconsistently between the two *Ec*Tsr chains in the asymmetric unit (Fig. 5G). Calculating f_o-f_c omit map density for both structures show clear support for our new *Se*Tsr ligand orientation, and an overlay with the *Ec*Tsr f_o-f_c omit map data indicates this orientation would also fit well the electron density for that structure (Fig. 5H-I). Thus, our new *Se*Tsr LBD structure is now the best resolved view of a Tsr-serine complex and revises our understanding of how the receptor mediates specific recognition of L-serine.

SeTsr LBD binds L-serine, but not NE or DHMA.

Despite a lack of chemotactic responses to NE and DHMA in our CIRA experiments (Fig. S2, Movie S5-6), our uncertainty lingered as to whether these neurotransmitters are sensed through Tsr. Prior work created theoretical models of NE and DHMA binding *Ec*Tsr at the L-serine site, and proposed this as the molecular mechanism underlying *E. coli* chemoattraction to these compounds (Orr et al., 2020). However, with our new experimentally-determined *Se*Tsr LBD crystal structure in hand, it is clear that the hydrogen bonding network is specific for L-serine (Fig. 5F, Movie S7), and we were doubtful such dissimilar ligands as NE or DHMA would be accommodated. We note that the amino acids that constitute the L-serine binding pocket are identical between *Se*Tsr and *Ec*Tsr (Fig. 5F-G), and so at the protein level *Se*Tsr LBD and *Ec*Tsr LBD should have similar molecular functions and ligand specificity.

We performed isothermal titration calorimetry (ITC) experiments, a gold-standard for measuring protein-ligand interactions, to study ligand recognition by *Se*Tsr LBD (Fig. 5J-L). As expected, L-serine produced a robust exothermic binding curve, exhibiting a K_D of

approximately 5 µM (Fig. 5J). This matches well with our observation of *S. enterica* chemoattraction requiring a source of L-serine at least 0.5-5 µM (Fig. 4D-E) and with prior ITC data with *Ec*Tsr LBD, which also reported a 5 µM K_D (Tajima et al., 2011). By comparison, neither NE nor DHMA showed any evidence of binding to *Se*Tsr LBD (Fig. 5K-L). These data confirm *Se*Tsr is as a receptor for L-serine, and not NE or DHMA, and further support the mechanism of Tsr-mediated serum chemoattraction to be through L-serine.

Bacteria with tsr genes perform serum chemoattraction

The biological distribution of Tsr chemoreceptors has not been previously characterized. We hypothesized that chemoattraction to serum, mediated through Tsr, might extend beyond *Salmonella* to other bacterial species. We applied our structural insights to define a motif consisting of the amino acids involved in L-serine recognition, and when we analyzed the genomes of Enterobacteriaceae genera such as *Escherichia*, *Citrobacter*, and *Enterobacter*, found that they too possess Tsr-like chemoreceptor genes (Fig. 5M). We next conducted a comprehensive search for chemoreceptor genes containing the L-serine recognition motif, resulting in the creation of a database containing all organisms that possess putative Tsr homologues (Fig. 5N, Data S1). The biological distribution of Tsr reveals the chemoreceptor to be widely conserved among Gammaproteobacteria, particularly within the families Enterobacteriaceae, Morganelliaceae, and Yersiniaceae (Fig. 5N). We identified that many WHO priority pathogens are among the species that have Tsr, leading us to suspect these pathogens and pathobionts also perform serum chemoattraction. To address this question, we performed CIRA analysis with human serum and the bacterial strains *E. coli* MG1655 and *C. koseri* BAA-895, a clinical isolate with uncharacterized chemotactic behavior. We find that both these strains exhibit chemoattraction to human serum on time scales and magnitudes similar to experiments with *Salmonella* (Fig. 6A-C). Based on these results, we infer serum chemoattraction to be a phenomenon common among Enterobacteriaceae species, and may also occur in Gammaproteobacteria priority pathogen genera such as *Serratia*, *Providencia*, *Morganella*, and *Proteus* (Fig. 5N).

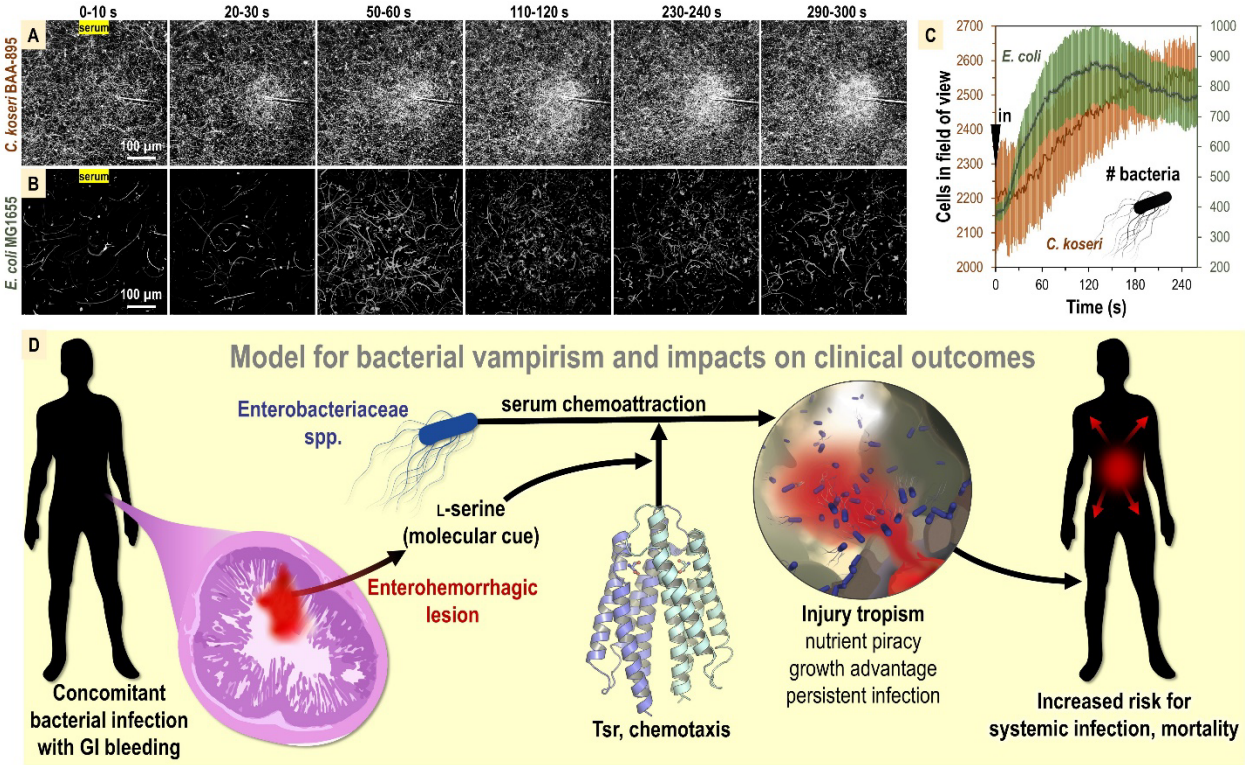

Fig. 6. Enterobacteriaceae possessing Tsr display chemoattraction to human serum. A-C. Response of *C. koseri* BAA-895 (n=3, 37° C) and *E. coli* MG1655 to human serum (n=3, 30° C), shown as max projections. D. Proposed model for bacterial vampirism and impact on clinical outcomes. Plotted data shown are means averaged over 1 s, and error is SEM. See also Movie S8, Movie S9, and Key Resources Table.

Discussion

The most probable outcome for gastrointestinal bacterial infections is that they are resolved by the immune system without chronic infection or lingering pathologies (Fig. 1). To understand why, in rare circumstances, infections do persist, become chronic, systemic, and life-threatening, we must uncover the mechanisms at the crossroads where pathogens divert from the routine course of infection and do something unusual. Chemotaxis is oft-regarded as a bacterial nutrient-seeking behavior (Keegstra et al., 2022; Matilla and Krell, 2018; Zhou et al., 2022). Our research reveals that chemotaxis may drive motile flagellated pathogens to colonize sites of bleeding, and, in doing so, pirate host nutrients from serum for growth advantages (Fig. 6D). We have coined the term ‘vampirism’ to describe this pathogenesis strategy, which aptly reflects that the bacteria feed on nutrients derived from serum. In the competitive ecological niche of the human GI tract, metabolites and metals made available through serum may provide vital nourishment to sustain

invading pathogens. Vampirism could underly the propensity of Enterobacteriaceae infections to cause bacteremia and be a mechanism by which GI pathogens preferentially colonize sites of injury (Aihara et al., 2014; Zhou et al., 2022).

We demonstrate here that human serum is a potent attractant for pathogenic Enterobacteriaceae and that these bacterial species use chemotaxis to recognize and swim toward serum sources (Fig. 2-3, Fig. 5-6). The response to human serum is rapid; the motile population restructures within 1-2 minutes of serum exposure and the bacterial cells increase in density to the point of saturation at the serum source (Fig. 2, Fig. 6). We expect that serum chemoattraction occurs through the cooperative action of multiple bacterial chemoreceptors that perceive several chemoattractant stimuli (Fig. 3A). Interestingly, we find that L-serine is one of the major drivers of serum chemoattraction, which is sensed through the chemoreceptor Tsr through a ligand-binding site that is highly optimized, and selective, for recognition of this amino acid (Fig. 4-5). The chemoreceptor Tsr is incredibly sensitive and can mount a chemoattractant response to a source as low as 500 nM L-serine, a concentration 480-times less than present in human serum (Fig. 4D-E). Interestingly, although the bacteria are attuned to L-serine, it appears to not be the major nutrient in serum that supports bacterial growth (Fig. 4H-K). Therefore, we consider L-serine to be a molecular cue that provides spatial information to the swimming bacteria to locate sources of human serum.

Having found that serum chemoattraction is a feature common among diverse *S. enterica* serovars isolated from human patients, as well as a representative strain of *E. coli* and a clinical isolate of *C. koseri*, we conclude this behavior is widespread among Enterobacteriaceae species and is associated with possessing the Tsr chemoreceptor (Fig. 2H-J, Fig. 5M-N, Fig. 6A-C). The phenomenon of pathogen serum chemoattraction aligns with previous studies that have identified an increased risk of bacterial infections originating from intestinal injuries (Satoh et al., n.d.; Vohra et al., 2020). Our advancements in comprehending the structural and mechanistic aspects of L-serine recognition can guide the development of new antibacterial medications that target the chemotaxis systems of Enterobacteriaceae to prevent persistent and systemic infections.

Roles for serum chemoattraction in pathogenesis

It is known that colitis presents enteric pathogens unique opportunities for nutrients and metabolic advantages (Litvak et al., 2019; Rivera-Chávez et al., 2016; Zhou et al., 2022).

Facultative anaerobic Enterobacteriaceae species restructure their metabolism to exploit luminal L-serine and gain a growth advantage in the inflamed gut (Kitamoto et al., 2020; Yoo and Byndloss, 2020). For colonizing the hostile environment of inflamed and injured tissue to be worthwhile, there must be fitness benefits for the pathogen that outweigh the deleterious effects of this microenvironment. Our data suggest that by localizing to sites of enteric bleeding pathogens are poised to feed on L-serine, and other metabolites, present in serum (Fig. 4H-K). These growth benefits may translate either to improved colonization of the intestinal lumen, tissue invasion, or, in rarer circumstances, to systemic infection through lymphatic or bloodstream entry.

We recognize that prior work has demonstrated bacterial growth can be impaired with pure human serum through complement-mediated killing, unless the strains are specifically adapted for bloodstream invasion (Cheng et al., 2019). In our investigation, the non-typhoidal *Salmonella* isolates, *E. coli*, and *C. koseri* strains we examined may serve as examples of serum-tolerant strains. Alternatively, a simpler explanation is that our study assessed responses to diluted human serum, whereas previous research evaluated bacterial growth in pure serum. Through our diffusion modeling of serum metabolites, we demonstrate that the concentration of effectors becomes significantly diluted just a few microns away from the source (Fig. 2B, Fig. 3A, Fig. S1). As a result, bactericidal factors present in serum may lose their potency. Notably, in neither our CIRA experiments with serum (Movie S1-S3, Movie S8-S9), nor growth assays with serum supplementation (Fig. 4H-K), do we observe evidence of bacterial killing. It is possible that previous investigations using pure serum provide a better representation of growth within the bloodstream (Cheng et al., 2019), while our experiments simulate the growth advantages experienced by luminal bacteria in close proximity to a source of GI bleeding.

In the context of *Salmonella* pathogenesis, it is interesting to note that diverse serovars, which vary in terms of host specificity and epidemiology, exhibit serum chemoattraction and have the ability to utilize serum as a nutrient (Fig. 2H-J, Fig. 4H-K). The specific nutrients responsible for the growth benefits derived from serum are not understood. However, one potential candidate is the presence of energy-rich glycoconjugates, which were previously implicated as nutrients in the inflamed intestine based on the upregulation of galactose utilization operons and the prevalence of lectin-positive stained tissue (Stecher et al., 2008). Enteric Peyer's patches are primary invasion sites for non-typhoidal *Salmonella*, and these structures are situated

close to vasculature that can be damaged through the pathogen's destruction of microfold (M) cells, causing localized bleeding (Shi et al., 2012). *S. enterica* Typhimurium uses the chemoreceptor Tsr to locate and invade Peyer's patches (Rivera-Chávez et al., 2016), which could involve L-serine chemoattraction originating from serum or necrotic cells. Although GI bleeding is relatively uncommon in *Salmonella* infections overall, it offlicts 60% of infected children under the age of five (White et al., 2019). Therefore, while we acknowledge that serum chemoattraction is unlikely to contribute to the routine pathogenesis strategy of *Salmonella*, the significant number of bacterial-induced GI bleeding cases, and the association between GI bleeding and bacterial invasion into the bloodstream, provide many opportunities for bacterial vampirism to be at play in clinical outcomes (Fig. 1)(Irving et al., 2021; Vohra et al., 2020; Weber et al., 2020).

Attraction to blood, serum, or plasma has been reported for some other bacteria, notably the blood-borne pathogens *Borrelia*, *Treponema*, and *Leptospirosis*, although the mechanisms that mediate attraction remain unknown (Haake and Levett, 2015; Lux and Shi, 2004; Sanderson et al., 2020; Tanno-Nakanishi et al., 2018). These bacteria do not possess the Tsr chemoreceptor. However, since blood contains numerous chemical components and proteinaceous factors, other chemoreceptors may drive the response. Similar mechanisms may occur for other non-Tsr-containing pathogens identified as exhibiting chemoattraction to serum components. For instance, gastric infection with the Epsilonproteobacteria *Helicobacter pylori* is associated with GI bleeding, and the pathogen is attracted to gastric lesions through chemoattraction to urea, which is present in serum near 5 mM (Aihara et al., 2014; Hanyu et al., 2019; Zhou et al., 2022).

Chemotaxis is a widely-conserved chemosensory system found in prokaryotes, known for its roles in nutrient acquisition and host colonization (Keegstra et al., 2022; Matilla et al., 2022; Zhou et al., 2022). Through mapping of chemoreceptor-chemoeffector interactions (Ortega et al., 2017), and the identification of conserved binding motifs that predict ligands recognized by chemoreceptor ligand-binding domains (Gavira et al., n.d.), the field has compiled an extensive collection of physicochemical stimuli perceived by bacterial chemotaxis systems (Matilla et al., 2022). However, to understand the roles of chemotaxis in human diseases, we must define the physiological landscape, and availability, of these chemoeffectors for bacteria within the human host environment. Our discovery that Enterobacteriaceae species exhibit rapid chemoattraction to human serum supports that GI bleeding is, in the microenvironment of enteric hemorrhagic

lesions, a source of L-serine accessible to luminal pathogens. This finding suggests there are undiscovered roles for previously identified chemoeffectors that drive pathogen colonization in specific environments relevant to human infections (Zhou et al., 2022).

Using CIRA for visualizing rapid chemotactic dynamics

The human gut is a highly dynamic environment where intestinal motility disrupts luminal gradients through frequent contractions, occurring approximately 3-12 times per minute (Sarna, 2010). In response to these transient gradients, chemotactic bacteria demonstrate rapid orchestration, leading to population aggregation or dispersion within seconds of encountering a new chemoeffector (Fig. 2-4) (Huang et al., 2017, 2015). To study how bacteria utilize chemotaxis in settings with dynamic and fleeting stimuli requires methods capable of observing responses on these fast timescales. One approach is CIRA, which is a microfluidics technique uniquely suited to provide such insights (Fig. 2-4). Injection of chemoeffectors has been used in prior work to study *H. pylori* chemoattraction to urea and the oxidant HOCl (Huang et al., 2015; Perkins et al., 2019), and chemorepulsion from acid (Howitt et al., 2011; Huang et al., 2017). In this study, we have expanded the utility of the CIRA approach in several ways. Firstly, we demonstrated its effectiveness in studying diverse pathogen species. Notably, this is the first investigation of the chemotactic behavior of *C. koseri*, and our approach holds potential for studying the chemotaxis systems of other WHO priority pathogens that have yet to be characterized (Fig. 6A,C). Secondly, we conducted direct comparisons of chemotactic responses between strains within the same experiment, exposed to the same chemoeffector source, and we introduce the radial distribution of the bacterial population as a sensitive and informative metric of bacterial localization (Fig. 2-4). Lastly, through modeling the microgradient generated by CIRA, we can estimate the local concentrations of effectors experienced by bacteria, permitting insight into how individual bacterial cells' sensing of effectors influences the chemotactic responses at the population level (Fig. 2, Fig. S1).

Limitations of this study

To model human infections, we employed bacterial strains that are human clinical isolates and utilized human serum as a treatment. However, it is important to note that our findings are derived from controlled experiments conducted in an *in vitro* system (CIRA) and *in vitro* cell

cultures. Therefore, the mechanism of serum chemoattraction mediated by Tsr sensing of L-serine requires further validation *in vivo*, and caution should be exercised in extrapolating our findings on chemosensing to the complex diseases of bacteremia and sepsis.

STAR Methods

RESOURCE AVAILABILITY

Lead contact

Further information and requests for resources and reagents should be directed to and will be fulfilled by the lead contact, Arden Baylink (arden.baylink@wsu.edu).

Materials availability

Strains and plasmids generated in this study will be made available upon request by the Lead Contact with a completed Materials Transfer Agreement.

Data availability

The crystal structure of L-serine-bound *Se*Tsr LBD has been deposited to the protein databank as PDB: 8FYV. Any additional information required to reanalyze the data reported in this paper is available from the Lead Contact upon request.

EXPERIMENTAL MODEL AND SUBJECT DETAILS

Bacterial strains

Strains of *S. enterica*, *E. coli*, and *C. koseri* used in this study are described in the Key Resources Table. To generate fluorescent strains, electrically-competent bacterial cultures were prepared through successive washing of cells with ice-cold 10 % glycerol, and then transformed by electroporation (Biorad GenePulser Xcell) with pxS vectors containing either sfGFP, or mPlum, and AmpR genes (Wiles et al., 2018). Transformants were isolated through growth on selective media and stored as glycerol stocks for subsequent use. To prepare motile bacterial cells for chemotaxis experiments, bacterial cultures were grown shaking overnight in 2-5 ml tryptone broth (TB) and 50 µg/ml ampicillin (TB+Amp) at 30˚ C or 37˚ C, as needed. The following day,

25 µl of overnight culture was used to inoculated 25 ml of fresh TB+Amp and grown shaking for 3-5 hours to reach optical density 600 (OD_{600}) of approximately 0.5. To better isolate responses to effectors of interest and remove confounding variables, such as pH variation and quorum-signaling molecules, we washed and exchanged the cells into a buffer of defined composition. Bacterial cultures were centrifuged at 1,500 g for 20 minutes and exchanged into a chemotaxis buffer (CB) containing 10 mM potassium phosphate (pH 7), 10 mM sodium lactate, and 100 µM EDTA. Cultures were diluted to approximately OD_{600} 0.2 and allowed to recover rocking gently for 30-60 minutes to become fully motile.

For *in vitro* growth analyses, *S. enterica* strains were grown in Luria-Bertani (LB) media shaking overnight at 37˚ C. The following day, cultures were pelleted by centrifugation and resuspended in a minimal media (MM) containing 47 mM Na_2HPO_4, 22 mM KH_2PO_4, 8 mM NaCl, 2mM $MgSO_4$, 0.4% glucose (w/v) 11.35 mM $(NH_4)_2SO_4$, 100 µM $CaCl_2$. 5 µl of the overnight cultures at 0.05 A_{600} were used to inoculate fresh solutions of 200 µl of MM, or additives diluted into MM (human serum or L-serine), in a 96-well microtiter plate. A plate reader was used to monitor cell growth while shaking at 37˚ via A_{600} readings every 5 minutes.

METHOD DETAILS

Chemosensory injection rig assay (CIRA)

Our CIRA system is based on prior work, with several notable changes to methodology, as described. (Howitt et al., 2011; Huang et al., 2015; Perkins et al., 2019). The CIRA apparatus was constructed using a pump for injection (either a refurbished Eppendorf Transjector 5246 or Femtojet 4i) and universal capillary holder, with solutions injected through Femtotip II glass microcapillaries (Eppendorf), and the microcapillary position controlled with a MP-285 micromanipulator (Sutter) at a 30˚ angle of attack. To generate a microgradient, a constant flow from the microcapillary was induced by applying compensation pressure (P_c) of 35 hPa. The stability of the microgradient under these conditions was determined with Alexa488 dye (ThermoFisher), and the flow was determined empirically with methylene blue dye to be approximately 300 femtoliters per minute at 30˚ C (Fig. S1). Pooled off-the-clot human serum was obtained from Innovative Research; serum was deidentified and had no additional chemical additives and is presumed to be fully active. Treatment solutions were filtered through a 0.2 µm

filter and injected as-is (serum) or diluted in CB (serine, aspartate, NE, DHMA). For each CIRA experiment, a fresh pond of 50 µl of motile bacteria was mounted open to air on a 10-well slide (MP Biomedicals), and the microcapillary containing the treatment of interest was lowered into the pond. Bacterial responses were imaged with an inverted Nikon Ti2 Eclipse microscope with an enclosed heated sample chamber. Temperature of experiments were at 37 ˚C, unless otherwise indicated.

CIRA microgradient modeling

Diffusion is modeled as a 3D process in which the diffusive species is slowly and continuously introduced at a fixed point in a large ambient fluid volume. The species to be injected is prepared at concentration M_s (typically in the range of 0.5 µM-5 mM) and is injected at a volume rate Q = 305.5 fl/min. The species diffuses into the ambient fluid with diffusion constant D. The governing equation for the diffusion of a species introduced continuously at a point source is:

$$C(r,t) = \frac{q}{4\pi D r} erfc \frac{r}{2\sqrt{Dt}}$$

where r is the distance from the point source, t is the time from injection initiation, and $q = M_s Q$ is the injection rate of the species, and C is the species concentration. We can simplify the presentation by defining a characteristic length scale r_0, characteristic time t_0, and dimensionless variables as:

$$r_0 = \frac{Q}{4\pi D}, t_0 = \frac{Q^2}{(8\pi)^2 D^3}, \bar{r} = \frac{r}{r_0}, \bar{t} = \frac{t}{t_0}.$$

Then, we have the diffusion-driven concentration model:

$$C(\bar{r},\bar{t}) = \frac{M_s}{\bar{r}} erfc \frac{\bar{r}}{\sqrt{\bar{t}}}$$

Representative diffusion coefficients are: A488, $4.00 \times 10^{-6}\ \mathrm{cm}^2/\mathrm{s}$; L-serine, $8.71 \times 10^{-6}\ \mathrm{cm}^2/\mathrm{s}$; L-aspartate, $9.35 \times 10^{-6}\ \mathrm{cm}^2/\mathrm{s}$. Due to the small injection rate, our assumption of

a point source leads to a model that is valid at distances $r \gg r_0 \sim 1$ nm and times $t \gg t_0 \sim 1$ ns. We also consider the total species quantity integrated along a viewing direction. The result is:

$$I(\bar{r}, \bar{t}) = 2M_s r_0 \int_0^\infty \frac{d\bar{z}}{\sqrt{\bar{z}^2 + \bar{r}^2}} erfc \frac{\sqrt{\bar{z}^2 + \bar{r}^2}}{\bar{t}}$$

where $\bar{z}$ is the unitless integration variable along the viewing direction. This integral was evaluated numerically by considering the sequence of points $z_k = \frac{k+1}{2} \Delta\bar{z}$ for $k = 1,2,3, \ldots$ and $\Delta\bar{z}$ some small interval. Then, we have the discrete integral approximation:

$$I(\bar{r}, \bar{z}) \approx 2M_s r_0 \Delta\bar{z} \sum_{k=1}^{N} (z_k^2 + \bar{r}^2)^{-1/2} erfc \frac{\sqrt{z_k^2 + \bar{r}^2}}{\bar{t}}.$$

Computations for this work used 1 μm steps extending out to $r = 500$ μm. That is, $\Delta\bar{z} = 1\ \mu\text{m}/r_0$ and $N = 500$.

Cloning and recombinant protein expression

Cloning of the *S. enterica* Tsr LBD construct for recombinant protein expression was performed as a service by Genscript Biotech Corp. The sequence of the periplasmic portion of the ligand-binding domain of *S. enterica* Typhimurium Tsr (gene *STM4533*), corresponding to residues 32-187 of the full-length protein, was encoded into a pet-30a(+) vector (Tsr-LBD-pet-30a(+)), at the NdeI and HindIII sites, with a short N-terminal TEV cleavage tag (MENLYFQ) such that the final expressed protein sequence was:

MENLYFQSLKNDKENFTVLQTIRQQQSALNATWVELLQTRNTLNRAGIRWMMDQSNIG
SGATVAELMQGATNTLKLTEKNWEQYEALPRDPRQSEAAFLEIKRTYDIYHGALAELIQ
LLGAGKINEFFDQPTQSYQDAFEKQYMAYMQQNDRLYDIAVEDNNS

Chemically-competent Rosetta BL21(DE3) *E. coli* (Millipore Sigma) were transformed by heat shock with the Tsr-LBD-pet-30a(+) vector, and transformants identified by growth on selective media containing 20 μg/ml (LB+Kan). Cells were grown overnight in 5 ml LB+Kan. The

following day, 1 ml of overnight culture was used to inoculate 1 L of fresh LB+Kan, and cultures were grown to OD_{600} 0.6-0.8 and induced with 0.4 mM isopropyl β-D-1-thiogalactopyranoside (IPTG). After growth for 3 H at 37˚ C cells, were harvested by centrifugation.

Purification of recombinant SeTsr LBD

The cell pellet was resuspended in a lysis buffer containing 50 mM Tris pH 7.5, 0.1 mM DTT, 1 mM EDTA, 5 mg DNAse I, and 1 cOmplete protease inhibitor tablet per 1 L of culture (Sigma Aldrich), and cells were lysed by sonication. After, the lysate was kept on ice and adjusted to 20 % ammonium sulfate saturation and stirred at 4˚ C for 30 minutes. Lysate was centrifuged at 15,000 rpm for 30 minutes in a Beckman ultracentrifuge. The soluble fraction was retained, and an ammonium precipitation trial was conducted; the 20-40% fraction contained the majority of the Tsr LBD protein and was used for subsequent purification. The protein solution was dialyzed for 16 hours against 4 L of 20 mM Tris, pH 7.5, 20 mM NaCl, and 0.1 mM EDTA, then run over an anion exchange column and FPLC (Akta). The purest fractions were pooled and treated with 0.3 mg/ml TEV protease, and the protein solution was dialyzed against 4 L of 50 mM Tris pH 8, 0.5 mM EDTA, and 1 mM EDTA for 48 h at 4˚ C. Subsequently, the cleaved protein solution was exchanged into a buffer of 50 mM Tris pH 7.5, 1 mM EDTA, and 150mM NaCl, and purified by gel filtration with an S200 column and FPLC. Pure protein fractions were pooled, concentrated to 7 mg/ml, and flash frozen in liquid N_2.

Protein crystallography

Initial crystallization trials of *Se*Tsr LBD were performed with either TEV-cleaved or uncleaved protein samples at 7 mg/ml with +/- 2 mM L-serine and using 96-well matrix screens set up with a Mosquito robot (SPT Labtech). We only observed crystal hits with the cleaved, serine-treated crystals, the best of which was 0.056 M sodium phosphate, 1.344 M potassium phosphate, pH 8.2. This condition was further optimized to be 1.5 µl *Se*Tsr LBD protein (7 mg/ml), 0.5 µl of 8 mM L-serine, and 1.5 µl 1.69 M potassium phosphate pH 9.7, grown via hanging drop vapor diffusion with a 1 ml reservoir of 1.69 M potassium phosphate pH 9.7 at 22˚ C. Attempts at using cryoprotectants were unsuccessful and resulted in crystals dissolving or diminished diffraction, so crystals were scooped directly from drops and flash frozen in liquid N_2. X-ray diffraction data were collected at the Berkeley Advanced Light Source (ALS) beamline 5.0.3.

Out of approximately 100 crystals examined, only one diffracted to high resolution and was not impacted by crystal twinning.

Data were indexed with DIALS (Winter et al., 2022), scaled with Aimless (Winn et al., 2011), and found to correspond well to space group $C2_1$. A conservative final resolution cutoff of 2.2 Å was applied on the basis of $CC_{1/2}$ >0.3 and completeness >50% in the highest resolution shell (Karplus and Diederichs, 2012).

The serine-bound *Ec*Tsr structure (PDB: 3atp) was utilized as a molecular replacement search model with Phaser-MR in Phenix (Adams et al., 2010) to solve the *Se*Tsr LBD dataset with five monomers in the asymmetric unit. 10% of the data were designated as R_{free} flags and the initial model was adjusted by setting all B-factors to 30 $Å^2$ and coordinates were randomized by 0.05 Å to reduce bias from the starting model. Subsequent model building with Coot (Emsley and Cowtan, 2004) and refinement with Phenix enabled placement of residues 42-182 and the serine ligand. However, residues 32-41 and 183-187 could not be resolved and were not modeled, causing the R/R_{free} values to being slightly elevated for a model of this resolution. Riding hydrogen atoms and translation, libration, screw refinement was applied and contributed to reduced R factors. The strongest remaining difference peak is along a symmetry axis. The final model R/R_{free} values were 24.1/25.8 %, with a 99th percentile all-atom MolProbity clashscore, and a 100th percentile overall MolProbity score (Davis et al., 2007). Crystallographic statistics are listed in Table S2. The structure was deposited to the protein data bank as entry 8FYV.

Isothermal titration calorimetry ligand binding studies (ITC)

ITC experiments were performed in 50 mM Tris, 150 mM NaCl, 1 mM EDTA, pH 7.5, at 25 °C. We dialyzed the protein into the experimental buffer and dissolved the small molecule ligands into the same buffer. Protein concentrations were ~50 μM; titrant concentrations were 500 μM. Samples were degassed prior to experiments. All experiments were performed on a MicroCal ITC-200 system (GE Healthcare), with the gain set to “low” and a syringe stir speed of 750 rpm. Titration data for the serine experiments were fit to a single-site binding model using the built-in ITC analysis software.

Mass Spectrometry

Determination of molar content of total serine in human serum samples was performed as a service through the University of Washington Mass Spectrometry Center. Samples were analyzed on the Waters TQ #1 instrument using a Thermo Hypersil Gold PFP column (2.1 x 100) with 0.1% heptafluorobutyric acid (HFBA) in water and acetonitrile.

QUANTIFICATION AND STATISTICAL ANALYSIS

Quantification of CIRA data

To determine relative numbers of cells over time, a ratio of fluorescence intensity per cell was calculated using ImageJ. Fluorescence intensity was used as a readout of relative cell count over time using the 'plot profile' function in ImageJ (Schneider et al., 2012). Cell numbers were normalized to a baseline of "100 %" at the start of treatment (shown as time 0). Distribution of the bacterial population was quantified through use of the 'radial profile' ImageJ plugin. Radial distribution data were normalized by setting the field of view periphery as the baseline of "1-fold," which we defined as 240 µm distance from the source. Images and videos shown were processed using the 'enhance contrast' function in ImageJ and adjusting intensity thresholds to normalize fluorescence intensity per cell across channels. For experiments with non-fluorescent cells, equivalent procedures were performed using phase contrast data and enumeration of cells over time using a Matlab-based tracking software (Perkins et al., 2019).

Statistical Analyses

Data from replicate experiments were averaged and interpreted on the basis of their mean, standard error of the mean, and effect sizes. Effect sizes for data are indicated as Cohen's *d* value:

$$\mathrm{d} = \frac{\mathrm{M}_1 - \mathrm{M}_2}{\sigma_{\mathrm{pooled}}}$$

where:

$$\sigma_{pooled} = \sqrt{\frac{{\sigma_1}^2 + {\sigma_2}^2}{2}}$$

Where relevant, *p*-values were calculated using either one-sided or unpaired two-sided tests, with significance determined at $p<0.05$:

$$t = \frac{\bar{x}_1 - \bar{x}_2}{\sqrt{s^2\left(\frac{1}{n_1} + \frac{1}{n_2}\right)}}$$

where:

$$s^2 = \frac{\sum_{i=1}^{n_1}(x_i - \bar{x}_1)^2 + \sum_{j=1}^{n_2}(x_j - \bar{x}_2)^2}{n_1 + n_2 - 2}$$

KEY RESOURCES TABLE

REAGENT OR RESOURCE	SOURCE	IDENTIFIER
Bacterial strains		
S. enterica Typhimurium		
IR715	(Rivera-Chávez et al., 2013b)	Nalidixic acid-derivative of ATCC 14028
FR13	(Rivera-Chávez et al., 2013b)	IR715 *cheY*::Tn*10* (Tet^R)
FR4	(Rivera-Chávez et al., 2013b)	IR715 tsr::pFR3 (Tet^R)
SARA1	(Beltran et al., 1991)	Isolated from patient in Mexico
S. enterica Newport		
M11018046001A	(Shariat et al., 2013b)	Isolated from patient in PA, USA
S. enterica Enteriditis		
05E01375	(Shariat et al., 2013a)	Isolated from patient in PA, USA
C. koseri		
BAA-895	ATCC	Human clinical isolate
E. coli		
MG1655	Karen Guillemin (UO)	Model of WT *E. coli*
K12	Millipore Sigma	Rosetta(DE3) BL21 derivative

Plasmids		
pXS-sfGFP	(Wiles et al., 2018)	pGEN-mcs with a modular sfGFP expression scaffold (Amp^R)
pXS-mPlum	(Wiles et al., 2018)	pGEN-mcs with a modular mPlum expression scaffold (Amp^R)
pET-30a(+)-*Se*TsrLBD	This study, Genscript	Vector for recombinant expression of *Se*Tsr LBD (Kan^R)
Chemicals and Recombinant Proteins		
*Se*Tsr LBD	This study	See Method Details
human serum	Innovative Research	ISERABOTCHI100ML
Deposited Data		
Crystal structure of *Se*Tsr LBD	This study	PDB code: 8FYV

Acknowledgements

Funding for this work was provided by NIAID under award numbers 1K99AI148587 and 4R00AI148587-03, and startup funding from Washington State University to AB. We thank Karen Guillemin (University of Oregon) for the Eppendorf Transjector used for the CIRA experiments. We thank Nikki Shariat (University of Georgia, Athens), Nkuchia Mikanatha and Pennsylvania NARMS and GenomeTrakr Programs, and Andreas Bäumler (University of California, Davis) for providing the *Salmonella* strains used in this work. Beamline 5.0.3 of the Advanced Light Source, a DOE Office of Science User Facility under Contract No. DE-AC02-05CH11231, is supported in part by the ALS-ENABLE program funded by the National Institutes of Health, National Institute of General Medical Sciences, grant P30 GM124169-01. All research on human samples was performed in accordance with, and approval of, the Institutional Biosafety Committee at Washington State University.

Author Contributions

A.B. and S.G. conducted the CIRA experiments. S.G. and Z.G. performed growth curve analyses with human serum and purified L-serine. A.B., S.G., and Z.G. performed the crystallographic analyses. T.A. performed the microgradient modeling. M.S. and M.J.H. performed the ITC experiments. All authors contributed to data analyses and writing of the manuscript.

Declaration of Interests

A.B. owns Amethyst Antimicrobials, LLC.

References

Adams, P.D., Afonine, P.V., Bunkóczi, G., Chen, V.B., Davis, I.W., Echols, N., Headd, J.J., Hung, L.-W., Kapral, G.J., Grosse-Kunstleve, R.W., McCoy, A.J., Moriarty, N.W., Oeffner, R., Read, R.J., Richardson, D.C., Richardson, J.S., Terwilliger, T.C., Zwart, P.H., 2010. PHENIX: a comprehensive Python-based system for macromolecular structure solution. Acta Cryst D 66, 213–221. https://doi.org/10.1107/S0907444909052925

Aihara, E., Closson, C., Matthis, A.L., Schumacher, M.A., Engevik, A.C., Zavros, Y., Ottemann, K.M., Montrose, M.H., 2014. Motility and Chemotaxis Mediate the Preferential Colonization of Gastric Injury Sites by Helicobacter pylori. PLOS Pathogens 10, e1004275. https://doi.org/10.1371/journal.ppat.1004275

Aljarad, Z., Mobayed, B.B., 2021. The mortality rate among patients with acute upper GI bleeding (with/without EGD) at Aleppo University Hospital: A retrospective study. Ann Med Surg (Lond) 71, 102958. https://doi.org/10.1016/j.amsu.2021.102958

Beltran, P., Plock, S.A., Smith, N.H., Whittam, T.S., Old, D.C., Selander, R.K., 1991. Reference collection of strains of the Salmonella typhimurium complex from natural populations. Microbiology 137, 601–606. https://doi.org/10.1099/00221287-137-3-601

Callahan, S.M., Dolislager, C.G., Johnson, J.G., n.d. The Host Cellular Immune Response to Infection by Campylobacter Spp. and Its Role in Disease. Infect Immun 89, e00116-21. https://doi.org/10.1128/IAI.00116-21

Cassidy, C.K., Himes, B.A., Sun, D., Ma, J., Zhao, G., Parkinson, J.S., Stansfeld, P.J., Luthey-Schulten, Z., Zhang, P., 2020. Structure and dynamics of the E. coli chemotaxis core signaling complex by cryo-electron tomography and molecular simulations. Commun Biol 3, 1–10. https://doi.org/10.1038/s42003-019-0748-0

Cheng, Z., Guo, C., Chen, Z., Yang, T., Zhang, J., Wang, J., Zhu, J., Li, D., Zhang, T., Li, H., Peng, B., Peng, X., 2019. Glycine, serine and threonine metabolism confounds efficacy of complement-mediated killing. Nat Commun 10, 3325. https://doi.org/10.1038/s41467-019-11129-5

Croxen, M.A., Finlay, B.B., 2010. Molecular mechanisms of Escherichia coli pathogenicity. Nat Rev Microbiol 8, 26–38. https://doi.org/10.1038/nrmicro2265

Davis, I.W., Leaver-Fay, A., Chen, V.B., Block, J.N., Kapral, G.J., Wang, X., Murray, L.W., Arendall, W.B., Snoeyink, J., Richardson, J.S., Richardson, D.C., 2007. MolProbity: all-atom contacts and structure validation for proteins and nucleic acids. Nucleic Acids Res 35, W375–W383. https://doi.org/10.1093/nar/gkm216

Donaldson, G.P., Lee, S.M., Mazmanian, S.K., 2016. Gut biogeography of the bacterial microbiota. Nat Rev Microbiol 14, 20–32. https://doi.org/10.1038/nrmicro3552

Emsley, P., Cowtan, K., 2004. Coot: model-building tools for molecular graphics. Acta Cryst D 60, 2126–2132. https://doi.org/10.1107/S0907444904019158

Ferrari, R.G., Rosario, D.K.A., Cunha-Neto, A., Mano, S.B., Figueiredo, E.E.S., Conte-Junior, C.A., 2019. Worldwide Epidemiology of Salmonella Serovars in Animal-Based Foods: a Meta-analysis. Appl Environ Microbiol 85, e00591-19. https://doi.org/10.1128/AEM.00591-19

Gavira, J.A., Gumerov, V.M., Rico-Jiménez, M., Petukh, M., Upadhyay, A.A., Ortega, A., Matilla, M.A., Zhulin, I.B., Krell, T., n.d. How Bacterial Chemoreceptors Evolve Novel Ligand Specificities. mBio 11, e03066-19. https://doi.org/10.1128/mBio.03066-19

Goren, I., Brom, A., Yanai, H., Dagan, A., Segal, G., Israel, A., 2020. Risk of bacteremia in hospitalised patients with inflammatory bowel disease: a 9-year cohort study. United European Gastroenterol J 8, 195–203. https://doi.org/10.1177/2050640619874524

Gumerov, V.M., Andrianova, E.P., Zhulin, I.B., 2021. Diversity of bacterial chemosensory systems. Current Opinion in Microbiology 61, 42–50. https://doi.org/10.1016/j.mib.2021.01.016

Haake, D.A., Levett, P.N., 2015. Leptospirosis in Humans. Curr Top Microbiol Immunol 387, 65–97. https://doi.org/10.1007/978-3-662-45059-8_5

Hanyu, H., Engevik, K.A., Matthis, A.L., Ottemann, K.M., Montrose, M.H., Aihara, E., 2019. Helicobacter pylori Uses the TlpB Receptor To Sense Sites of Gastric Injury. Infect Immun 87, e00202-19. https://doi.org/10.1128/IAI.00202-19

Hashimoto, K., Fukushima, T., Shimizu, E., Komatsu, N., Watanabe, H., Shinoda, N., Nakazato, M., Kumakiri, C., Okada, S., Hasegawa, H., Imai, K., Iyo, M., 2003. Decreased Serum Levels of D-Serine in Patients With Schizophrenia: Evidence in Support of the N-Methyl-D-Aspartate Receptor Hypofunction Hypothesis of Schizophrenia. Archives of General Psychiatry 60, 572–576. https://doi.org/10.1001/archpsyc.60.6.572

He, Q., Zhang, N., Liang, Q., Wang, Z., Chen, P., Song, Y., Zhou, Z., Wei, Y., Duan, Y., Wang, B., Qin, P., Qin, X., Xu, X., 2022. Serum Serine and the Risk of All-Cause Mortality: A Nested Case-Control Study From the China Stroke Primary Prevention Trial (CSPPT). Frontiers in Nutrition 9.

Howitt, M.R., Lee, J.Y., Lertsethtakarn, P., Vogelmann, R., Joubert, L.-M., Ottemann, K.M., Amieva, M.R., 2011. ChePep Controls Helicobacter pylori Infection of the Gastric Glands and Chemotaxis in the Epsilonproteobacteria. mBio 2, e00098-11. https://doi.org/10.1128/mBio.00098-11

Huang, A.H., Liu, Y., Hsien, Y.-C., Hsu, T.-C., Yen, D., Hsu, W.-T., Lin, H.-Y., Chen, S.-C., Lee, C.-C., 2021. Survival Impact and Clinical Predictors of Acute Gastrointestinal Bleeding in Patients With Bloodstream Infection. J Intensive Care Med 36, 63–69. https://doi.org/10.1177/0885066619884896

Huang, J.Y., Sweeney, E.G., Guillemin, K., Amieva, M.R., 2017. Multiple Acid Sensors Control Helicobacter pylori Colonization of the Stomach. PLOS Pathogens 13, e1006118. https://doi.org/10.1371/journal.ppat.1006118

Huang, J.Y., Sweeney, E.G., Sigal, M., Zhang, H.C., Remington, S.J., Cantrell, M.A., Kuo, C.J., Guillemin, K., Amieva, M.R., 2015. Chemodetection and Destruction of Host Urea Allows Helicobacter pylori to Locate the Epithelium. Cell Host Microbe 18, 147–156. https://doi.org/10.1016/j.chom.2015.07.002

Irving, P.M., Lusignan, S. de, Tang, D., Nijher, M., Barrett, K., 2021. Risk of common infections in people with inflammatory bowel disease in primary care: a population-based cohort study. BMJ Open Gastroenterology 8, e000573. https://doi.org/10.1136/bmjgast-2020-000573

Jakuszeit, T., Lindsey-Jones, J., Peaudecerf, F.J., Croze, O.A., 2021. Migration and accumulation of bacteria with chemotaxis and chemokinesis. Eur Phys J E Soft Matter 44, 32. https://doi.org/10.1140/epje/s10189-021-00009-w

Karplus, P.A., Diederichs, K., 2012. Linking Crystallographic Model and Data Quality. Science 336, 1030–1033. https://doi.org/10.1126/science.1218231

Kearns, D.B., 2010. A field guide to bacterial swarming motility. Nat Rev Microbiol 8, 634–644. https://doi.org/10.1038/nrmicro2405

Keegstra, J.M., Carrara, F., Stocker, R., 2022. The ecological roles of bacterial chemotaxis. Nat Rev Microbiol 1–14. https://doi.org/10.1038/s41579-022-00709-w

Kim, B.S.M., Li, B.T., Engel, A., Samra, J.S., Clarke, S., Norton, I.D., Li, A.E., 2014. Diagnosis of gastrointestinal bleeding: A practical guide for clinicians. World J Gastrointest Pathophysiol 5, 467–478. https://doi.org/10.4291/wjgp.v5.i4.467

Kitamoto, S., Alteri, C.J., Rodrigues, M., Nagao-Kitamoto, H., Sugihara, K., Himpsl, S.D., Bazzi, M., Miyoshi, M., Nishioka, T., Hayashi, A., Morhardt, T.L., Kuffa, P., Grasberger, H., El-Zaatari, M., Bishu, S., Ishii, C., Hirayama, A., Eaton, K.A., Dogan, B., Simpson, K.W., Inohara, N., Mobley, H.L.T., Kao, J.Y., Fukuda, S., Barnich, N., Kamada, N., 2020. Dietary L-serine confers a competitive fitness advantage to Enterobacteriaceae in the inflamed gut. Nat Microbiol 5, 116–125. https://doi.org/10.1038/s41564-019-0591-6

Kopin, I.J., Lake, R.C., Ziegler, M., 1978. Plasma levels of norepinephrine. Ann Intern Med 88, 671–680. https://doi.org/10.7326/0003-4819-88-5-671

Ligthart, K., Belzer, C., de Vos, W.M., Tytgat, H.L.P., 2020. Bridging Bacteria and the Gut: Functional Aspects of Type IV Pili. Trends in Microbiology, Special Issue: Infection Biology in the Age of the Microbiome 28, 340–348. https://doi.org/10.1016/j.tim.2020.02.003

Litvak, Y., Mon, K.K.Z., Nguyen, H., Chanthavixay, G., Liou, M., Velazquez, E.M., Kutter, L., Alcantara, M.A., Byndloss, M.X., Tiffany, C.R., Walker, G.T., Faber, F., Zhu, Y., Bronner, D.N., Byndloss, A.J., Tsolis, R.M., Zhou, H., Bäumler, A.J., 2019. Commensal Enterobacteriaceae Protect against Salmonella Colonization through Oxygen Competition. Cell Host & Microbe 25, 128-139.e5. https://doi.org/10.1016/j.chom.2018.12.003

Lux, R., Shi, W., 2004. Chemotaxis-guided Movements in Bacteria. Critical Reviews in Oral Biology & Medicine 15, 207–220. https://doi.org/10.1177/154411130401500404

Matilla, M.A., Krell, T., 2018. The effect of bacterial chemotaxis on host infection and pathogenicity. FEMS Microbiol Rev 42. https://doi.org/10.1093/femsre/fux052

Matilla, M.A., Velando, F., Martín-Mora, D., Monteagudo-Cascales, E., Krell, T., 2022. A catalogue of signal molecules that interact with sensor kinases, chemoreceptors and transcriptional regulators. FEMS Microbiology Reviews 46, fuab043. https://doi.org/10.1093/femsre/fuab043

Medicine, C. for V., 2020. Get the Facts about Salmonella. FDA.

Mestas, J., Hughes, C.C.W., 2004. Of Mice and Not Men: Differences between Mouse and Human Immunology. The Journal of Immunology 172, 2731–2738. https://doi.org/10.4049/jimmunol.172.5.2731

Miller, D.E., Ferreira, C.R., Scott, A.I., Chang, I.J., 2020. Pharmacokinetics of oral l-serine supplementation in a single patient. Molecular Genetics and Metabolism Reports 24, 100607. https://doi.org/10.1016/j.ymgmr.2020.100607

Minasyan, H., 2019. Sepsis: mechanisms of bacterial injury to the patient. Scandinavian Journal of Trauma, Resuscitation and Emergency Medicine 27, 19. https://doi.org/10.1186/s13049-019-0596-4

Moledina, S.M., Komba, E., 2017. Risk factors for mortality among patients admitted with upper gastrointestinal bleeding at a tertiary hospital: a prospective cohort study. BMC Gastroenterology 17, 165. https://doi.org/10.1186/s12876-017-0712-8

Munekawa, C., Okada, H., Hamaguchi, M., Habu, M., Kurogi, K., Murata, H., Ito, M., Fukui, M., 2022. Fasting plasma glucose level in the range of 90–99 mg/dL and the risk of the onset of type 2 diabetes: Population based Panasonic cohort study 2. J Diabetes Investig 13, 453–459. https://doi.org/10.1111/jdi.13692

Murdoch, C.C., Skaar, E.P., 2022. Nutritional immunity: the battle for nutrient metals at the host–pathogen interface. Nat Rev Microbiol 20, 657–670. https://doi.org/10.1038/s41579-022-00745-6

Murray, C.J., Ikuta, K.S., Sharara, F., Swetschinski, L., Robles Aguilar, G., Gray, A., Han, C., Bisignano, C., Rao, P., Wool, E., Johnson, S.C., Browne, A.J., Chipeta, M.G., Fell, F., Hackett, S., Haines-Woodhouse, G., Kashef Hamadani, B.H., Kumaran, E.A.P., McManigal, B., Agarwal, R., Akech, S., Albertson, S., Amuasi, J., Andrews, J., Aravkin, A., Ashley, E., Bailey, F., Baker, S., Basnyat, B., Bekker, A., Bender, R., Bethou, A., Bielicki, J., Boonkasidecha, S., Bukosia, J., Carvalheiro, C., Castañeda-Orjuela, C., Chansamouth, V., Chaurasia, S., Chiurchiù, S., Chowdhury, F., Cook, A.J., Cooper, B., Cressey, T.R., Criollo-Mora, E., Cunningham, M., Darboe, S., Day, N.P.J., De Luca, M., Dokova, K., Dramowski, A., Dunachie, S.J., Eckmanns, T., Eibach, D., Emami, A., Feasey, N., Fisher-Pearson, N., Forrest, K., Garrett, D., Gastmeier, P., Giref, A.Z., Greer, R.C., Gupta, V., Haller, S., Haselbeck, A., Hay, S.I., Holm, M., Hopkins, S., Iregbu, K.C., Jacobs, J., Jarovsky, D., Javanmardi, F., Khorana, M., Kissoon, N., Kobeissi, E., Kostyanev, T., Krapp, F., Krumkamp, R., Kumar, A., Kyu, H.H., Lim, C., Limmathurotsakul, D., Loftus, M.J., Lunn, M., Ma, J., Mturi, N., Munera-Huertas, T., Musicha, P., Mussi-Pinhata, M.M., Nakamura, T., Nanavati, R., Nangia, S., Newton, P., Ngoun, C., Novotney, A., Nwakanma, D., Obiero, C.W., Olivas-Martinez, A., Olliaro, P., Ooko, E., Ortiz-Brizuela, E., Peleg, A.Y., Perrone, C., Plakkal, N., Ponce-de-Leon, A., Raad, M., Ramdin, T., Riddell, A., Roberts, T., Robotham, J.V., Roca, A., Rudd, K.E., Russell, N., Schnall, J., Scott, J.A.G., Shivamallappa, M., Sifuentes-Osornio, J., Steenkeste, N., Stewardson, A.J., Stoeva, T., Tasak, N., Thaiprakong, A., Thwaites, G., Turner, C., Turner, P., van Doorn, H.R., Velaphi, S., Vongpradith, A., Vu, H., Walsh, T., Waner, S., Wangrangsimakul, T., Wozniak, T., Zheng, P., Sartorius, B., Lopez, A.D., Stergachis, A., Moore, C., Dolecek, C., Naghavi, M., 2022. Global burden of bacterial antimicrobial resistance in 2019: a systematic analysis. The Lancet 399, 629–655. https://doi.org/10.1016/S0140-6736(21)02724-0

Namdee, K., Carrasco-Teja, M., Fish, M.B., Charoenphol, P., Eniola-Adefeso, O., 2015. Effect of Variation in hemorheology between human and animal blood on the binding efficacy of vascular-targeted carriers. Sci Rep 5, 11631. https://doi.org/10.1038/srep11631

Orr, A.A., Yang, J., Sule, N., Chawla, R., Hull, K.G., Zhu, M., Romo, D., Lele, P.P., Jayaraman, A., Manson, M.D., Tamamis, P., 2020. Molecular Mechanism for Attractant Signaling to

DHMA by E. coli Tsr. Biophysical Journal 118, 492–504. https://doi.org/10.1016/j.bpj.2019.11.3382

Ortega, Á., Zhulin, I.B., Krell, T., 2017. Sensory Repertoire of Bacterial Chemoreceptors. Microbiology and Molecular Biology Reviews 81, e00033-17. https://doi.org/10.1128/MMBR.00033-17

Pasupuleti, S., Sule, N., Cohn, W.B., MacKenzie, D.S., Jayaraman, A., Manson, M.D., 2014. Chemotaxis of Escherichia coli to norepinephrine (NE) requires conversion of NE to 3,4-dihydroxymandelic acid. J Bacteriol 196, 3992–4000. https://doi.org/10.1128/JB.02065-14

Paul, D.S., Walton, F.S., Saunders, R.J., Stýblo, M., 2011. Characterization of the Impaired Glucose Homeostasis Produced in C57BL/6 Mice by Chronic Exposure to Arsenic and High-Fat Diet. Environ Health Perspect 119, 1104–1109. https://doi.org/10.1289/ehp.1003324

Perkins, A., Tudorica, D.A., Amieva, M.R., Remington, S.J., Guillemin, K., 2019. Helicobacter pylori senses bleach (HOCl) as a chemoattractant using a cytosolic chemoreceptor. PLoS Biol 17, e3000395. https://doi.org/10.1371/journal.pbio.3000395

Perkins, A., Tudorica, D.A., Teixeira, R.D., Schirmer, T., Zumwalt, L., Ogba, O.M., Cassidy, C.K., Stansfeld, P.J., Guillemin, K., 2021. A Bacterial Inflammation Sensor Regulates c-di-GMP Signaling, Adhesion, and Biofilm Formation. mBio 12, e00173-21. https://doi.org/10.1128/mBio.00173-21

Pitkänen, H.T., Oja, S.S., Kemppainen, K., Seppä, J.M., Mero, A.A., 2003. Serum amino acid concentrations in aging men and women. Amino Acids 24, 413–421. https://doi.org/10.1007/s00726-002-0338-0

Rivera-Chávez, F., Lopez, C.A., Zhang, L.F., García-Pastor, L., Chávez-Arroyo, A., Lokken, K.L., Tsolis, R.M., Winter, S.E., Bäumler, A.J., 2016. Energy Taxis toward Host-Derived Nitrate Supports a Salmonella Pathogenicity Island 1-Independent Mechanism of Invasion. mBio 7, e00960-16. https://doi.org/10.1128/mBio.00960-16

Rivera-Chávez, F., Winter, S.E., Lopez, C.A., Xavier, M.N., Winter, M.G., Nuccio, S.-P., Russell, J.M., Laughlin, R.C., Lawhon, S.D., Sterzenbach, T., Bevins, C.L., Tsolis, R.M., Harshey, R., Adams, L.G., Bäumler, A.J., 2013a. Salmonella Uses Energy Taxis to Benefit from Intestinal Inflammation. PLOS Pathogens 9, e1003267. https://doi.org/10.1371/journal.ppat.1003267

Rivera-Chávez, F., Winter, S.E., Lopez, C.A., Xavier, M.N., Winter, M.G., Nuccio, S.-P., Russell, J.M., Laughlin, R.C., Lawhon, S.D., Sterzenbach, T., Bevins, C.L., Tsolis, R.M., Harshey, R., Adams, L.G., Bäumler, A.J., 2013b. Salmonella uses energy taxis to benefit from intestinal inflammation. PLoS Pathog 9, e1003267. https://doi.org/10.1371/journal.ppat.1003267

Saltzman, J.R., 2022. Approach to acute upper gastrointestinal bleeding in adults.

Sanderson, V.P., Mainprize, I.L., Verzijlenberg, L., Khursigara, C.M., Wills, M.K.B., 2020. The Platelet Fraction Is a Novel Reservoir to Detect Lyme Borrelia in Blood. Biology (Basel) 9, 366. https://doi.org/10.3390/biology9110366

Sarna, S.K., 2010. Colonic Motility: From Bench Side to Bedside, Integrated Systems Physiology: From Molecule to Function to Disease. Morgan & Claypool Life Sciences, San Rafael (CA).

Satoh, K., Okuyama, M., Furuya, T., Irie, Y., Nakae, H., n.d. Severe Sepsis Caused by Bacteria That Entered via the Intestinal Tract: A Case of Crohn's Disease in a Child. Cureus 12, e9822. https://doi.org/10.7759/cureus.9822

Scales, B.S., Huffnagle, G.B., 2013. The Microbiome in Wound Repair and Tissue Fibrosis. J Pathol 229, 323–331. https://doi.org/10.1002/path.4118

Schneider, C.A., Rasband, W.S., Eliceiri, K.W., 2012. NIH Image to ImageJ: 25 years of image analysis. Nat Methods 9, 671–675. https://doi.org/10.1038/nmeth.2089

Shariat, N., DiMarzio, M.J., Yin, S., Dettinger, L., Sandt, C.H., Lute, J.R., Barrangou, R., Dudley, E.G., 2013a. The combination of CRISPR-MVLST and PFGE provides increased discriminatory power for differentiating human clinical isolates of Salmonella enterica subsp. enterica serovar Enteritidis. Food Microbiology 34, 164–173. https://doi.org/10.1016/j.fm.2012.11.012

Shariat, N., Kirchner, M.K., Sandt, C.H., Trees, E., Barrangou, R., Dudley, E.G., 2013b. Subtyping of Salmonella enterica Serovar Newport Outbreak Isolates by CRISPR-MVLST and Determination of the Relationship between CRISPR-MVLST and PFGE Results. J Clin Microbiol 51, 2328–2336. https://doi.org/10.1128/JCM.00608-13

Shi, Z., Cai, Z., Yu, J., Zhang, T., Zhao, S., Smeds, E., Zhang, Q., Wang, F., Zhao, C., Fu, S., Ghosh, S., Zhang, D., 2012. Toll-like Receptor 11 (TLR11) Prevents Salmonella Penetration into the Murine Peyer Patches *. Journal of Biological Chemistry 287, 43417–43423. https://doi.org/10.1074/jbc.M112.411009

Stecher, B., Barthel, M., Schlumberger, M.C., Haberli, L., Rabsch, W., Kremer, M., Hardt, W.-D., 2008. Motility allows S. Typhimurium to benefit from the mucosal defence. Cellular Microbiology 10, 1166–1180. https://doi.org/10.1111/j.1462-5822.2008.01118.x

Steuer, A.E., Schmidhauser, C., Tingelhoff, E.H., Schmid, Y., Rickli, A., Kraemer, T., Liechti, M.E., 2016. Impact of Cytochrome P450 2D6 Function on the Chiral Blood Plasma Pharmacokinetics of 3,4-Methylenedioxymethamphetamine (MDMA) and Its Phase I and II Metabolites in Humans. PLOS ONE 11, e0150955. https://doi.org/10.1371/journal.pone.0150955

Tacconelli, E., Carrara, E., Savoldi, A., Harbarth, S., Mendelson, M., Monnet, D.L., Pulcini, C., Kahlmeter, G., Kluytmans, J., Carmeli, Y., Ouellette, M., Outterson, K., Patel, J., Cavaleri, M., Cox, E.M., Houchens, C.R., Grayson, M.L., Hansen, P., Singh, N., Theuretzbacher, U., Magrini, N., Aboderin, A.O., Al-Abri, S.S., Awang Jalil, N., Benzonana, N., Bhattacharya, S., Brink, A.J., Burkert, F.R., Cars, O., Cornaglia, G., Dyar, O.J., Friedrich, A.W., Gales, A.C., Gandra, S., Giske, C.G., Goff, D.A., Goossens, H., Gottlieb, T., Guzman Blanco, M., Hryniewicz, W., Kattula, D., Jinks, T., Kanj, S.S., Kerr, L., Kieny, M.-P., Kim, Y.S., Kozlov, R.S., Labarca, J., Laxminarayan, R., Leder, K., Leibovici, L., Levy-Hara, G., Littman, J., Malhotra-Kumar, S., Manchanda, V., Moja, L., Ndoye, B., Pan, A., Paterson, D.L., Paul, M., Qiu, H., Ramon-Pardo, P., Rodríguez-Baño, J., Sanguinetti, M., Sengupta, S., Sharland, M., Si-Mehand, M., Silver, L.L., Song, W., Steinbakk, M., Thomsen, J., Thwaites, G.E., van der Meer, J.W., Van Kinh, N., Vega, S., Villegas, M.V., Wechsler-Fördös, A., Wertheim, H.F.L., Wesangula, E., Woodford, N., Yilmaz, F.O., Zorzet, A., 2018. Discovery, research, and development of new antibiotics: the WHO priority list of antibiotic-resistant bacteria and tuberculosis. The Lancet Infectious Diseases 18, 318–327. https://doi.org/10.1016/S1473-3099(17)30753-3

Tajima, H., Imada, K., Sakuma, M., Hattori, F., Nara, T., Kamo, N., Homma, M., Kawagishi, I., 2011. Ligand Specificity Determined by Differentially Arranged Common Ligand-binding Residues in Bacterial Amino Acid Chemoreceptors Tsr and Tar*. Journal of Biological Chemistry 286, 42200–42210. https://doi.org/10.1074/jbc.M111.221887

Tanno-Nakanishi, M., Kikuchi, Y., Kokubu, E., Yamada, S., Ishihara, K., 2018. Treponema denticola transcriptional profiles in serum-restricted conditions. FEMS Microbiology Letters 365, fny171. https://doi.org/10.1093/femsle/fny171

Tsolis, R.M., Townsend, S.M., Miao, E.A., Miller, S.I., Ficht, T.A., Adams, L.G., Bäumler, A.J., 1999. Identification of a Putative Salmonella enterica Serotype Typhimurium Host Range Factor with Homology to IpaH and YopM by Signature-Tagged Mutagenesis. Infection and Immunity 67, 6385–6393. https://doi.org/10.1128/IAI.67.12.6385-6393.1999

Vohra, I., Attar, B., Sharma, S., Katiyar, V., Jaiswal, M., 2020. P129 INPATIENT OUTCOMES OF SEPSIS IN INFLAMMATORY BOWEL DISEASE PATIENTS: A 2016 NATIONWIDE INPATIENT SAMPLE ANALYSIS. Inflammatory Bowel Diseases 26, S25–S26. https://doi.org/10.1093/ibd/zaa010.059

Wadhwa, N., Berg, H.C., 2022. Bacterial motility: machinery and mechanisms. Nat Rev Microbiol 20, 161–173. https://doi.org/10.1038/s41579-021-00626-4

Weber, A., Sauk, J., Limketkai, B., 2020. P130 LEADING CAUSES OF MORTALITY IN INFLAMMATORY BOWEL DISEASE: A NATIONWIDE ANALYSIS. Gastroenterology 158, S41–S42. https://doi.org/10.1053/j.gastro.2019.11.122

Westerman, T.L., McClelland, M., Elfenbein, J.R., 2021. YeiE Regulates Motility and Gut Colonization in Salmonella enterica Serotype Typhimurium. mBio 12, e03680-20. https://doi.org/10.1128/mBio.03680-20

White, A.E., Ciampa, N., Chen, Y., Kirk, M., Nesbitt, A., Bruce, B.B., Walter, E.S., 2019. Characteristics of Campylobacter, Salmonella Infections and Acute Gastroenteritis in Older Adults in Australia, Canada, and the United States. Clin Infect Dis 69, 1545–1552. https://doi.org/10.1093/cid/ciy1142

Wiles, T.J., Wall, E.S., Schlomann, B.H., Hay, E.A., Parthasarathy, R., Guillemin, K., 2018. Modernized Tools for Streamlined Genetic Manipulation and Comparative Study of Wild and Diverse Proteobacterial Lineages. mBio 9, e01877-18. https://doi.org/10.1128/mBio.01877-18

Winn, M.D., Ballard, C.C., Cowtan, K.D., Dodson, E.J., Emsley, P., Evans, P.R., Keegan, R.M., Krissinel, E.B., Leslie, A.G.W., McCoy, A., McNicholas, S.J., Murshudov, G.N., Pannu, N.S., Potterton, E.A., Powell, H.R., Read, R.J., Vagin, A., Wilson, K.S., 2011. Overview of the CCP4 suite and current developments. Acta Cryst D 67, 235–242. https://doi.org/10.1107/S0907444910045749

Winter, G., Beilsten□Edmands, J., Devenish, N., Gerstel, M., Gildea, R.J., McDonagh, D., Pascal, E., Waterman, D.G., Williams, B.H., Evans, G., 2022. DIALS as a toolkit. Protein Sci 31, 232–250. https://doi.org/10.1002/pro.4224

Winter, S.E., Thiennimitr, P., Winter, M.G., Butler, B.P., Huseby, D.L., Crawford, R.W., Russell, J.M., Bevins, C.L., Adams, L.G., Tsolis, R.M., Roth, J.R., Bäumler, A.J., 2010. Gut inflammation provides a respiratory electron acceptor for Salmonella. Nature 467, 426–429. https://doi.org/10.1038/nature09415

Yoo, W., Byndloss, M.X., 2020. How to thrive in the inflamed gut. Nat Microbiol 5, 10–11. https://doi.org/10.1038/s41564-019-0642-z

Zhao, F., Cheng, L., Shao, Q., Chen, Z., Lv, X., Li, J., He, L., Sun, Y., Ji, Q., Lu, P., Ji, Y., Ji, J., 2020. Characterization of serum small extracellular vesicles and their small RNA contents across humans, rats, and mice. Sci Rep 10, 4197. https://doi.org/10.1038/s41598-020-61098-9

Zhou, B., Szymanski, C.M., Baylink, A., 2022. Bacterial chemotaxis in human diseases. Trends in Microbiology. https://doi.org/10.1016/j.tim.2022.10.007

Supplementary Information

Supplemental Figures

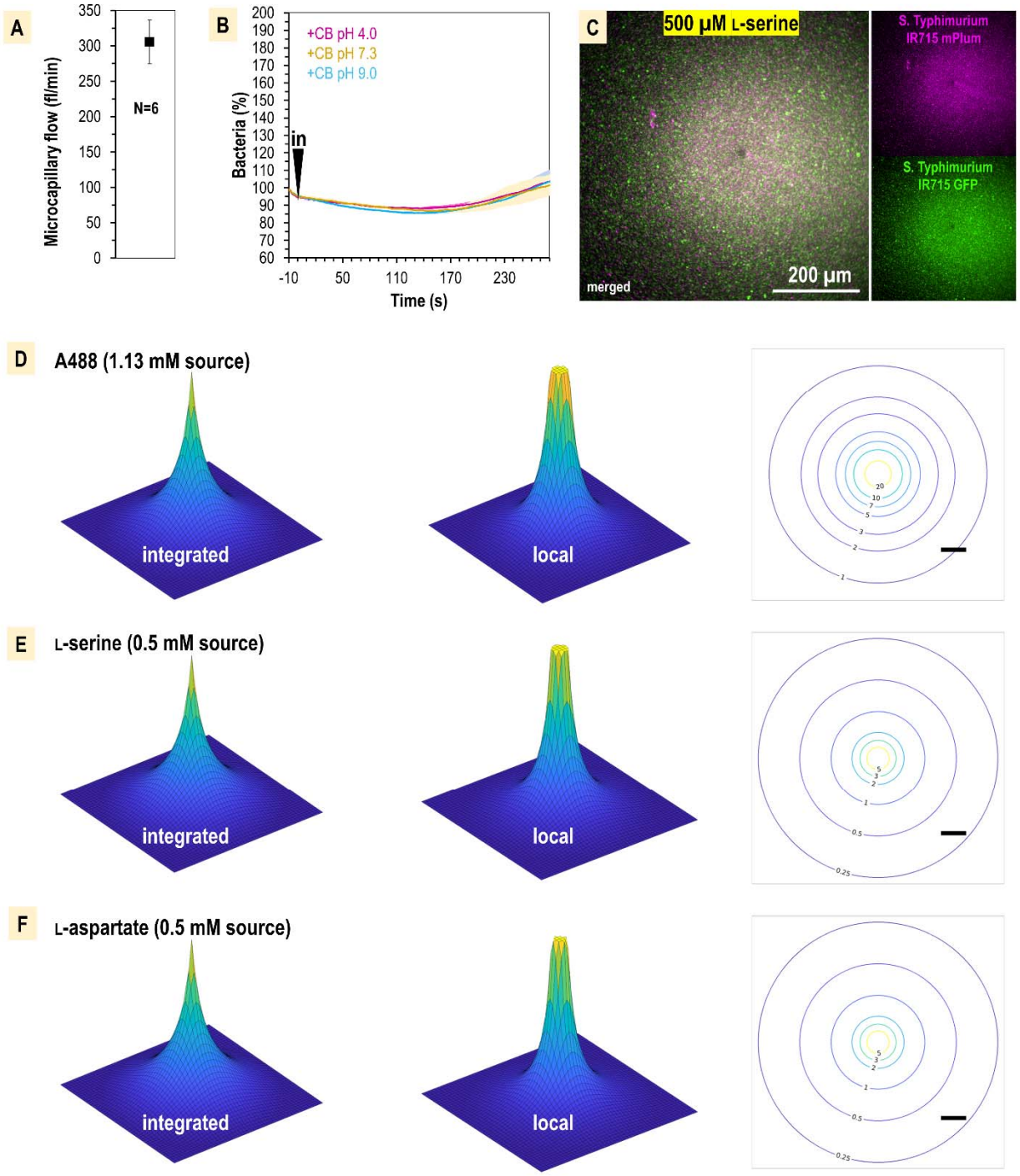

Fig. S1. CIRA experimentation controls and microgradient modeling. A. Average injection flow of treatment solution from the glass microcapillary. Flow was measured through injection of known concentrations of methylene blue dye, diluted in CB, into a 50 µl pond of CB over 20 minutes. After treatments, the absorbance of solutions was measured at 665 nm and quantified based on a standard curve. Applying a compensation pressure of 35 hPa resulted in an average

flow of 305.5 fl/min ± 31. B. CIRA localization in response to treatments of buffered CB of different pH. C. Comparison of responses of GFP versus mPlum strains using CIRA. D-F. Model of the CIRA microgradient for effectors relevant to this study. Topology maps of 1 mm x 1 mm size are shown for each microgradient in an 'integrated' format, which models what is seen by eye from the bottom-up view of the microscopy plane (left), or as the local concentration that would be experienced by a bacterium at a given distance (center). A plane through the center of the treatment sphere is shown (right), with relative concentrations experienced at a given distance expressed in nM units (scale bar is 100 µm).

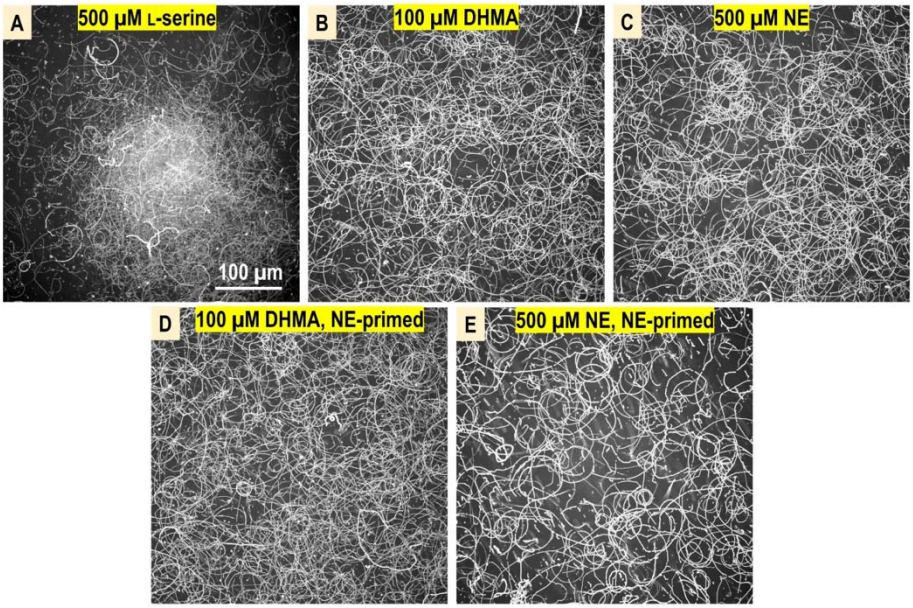

Fig. S2. Comparison of responses to L-serine versus DHMA and NE. Shown are max projections from CIRA experiments over a 10 s time period following 300 s of treatments as shown. Experiments D-E utilized cells that were primed with 5 µM NE for 3 hours prior to experimentation.

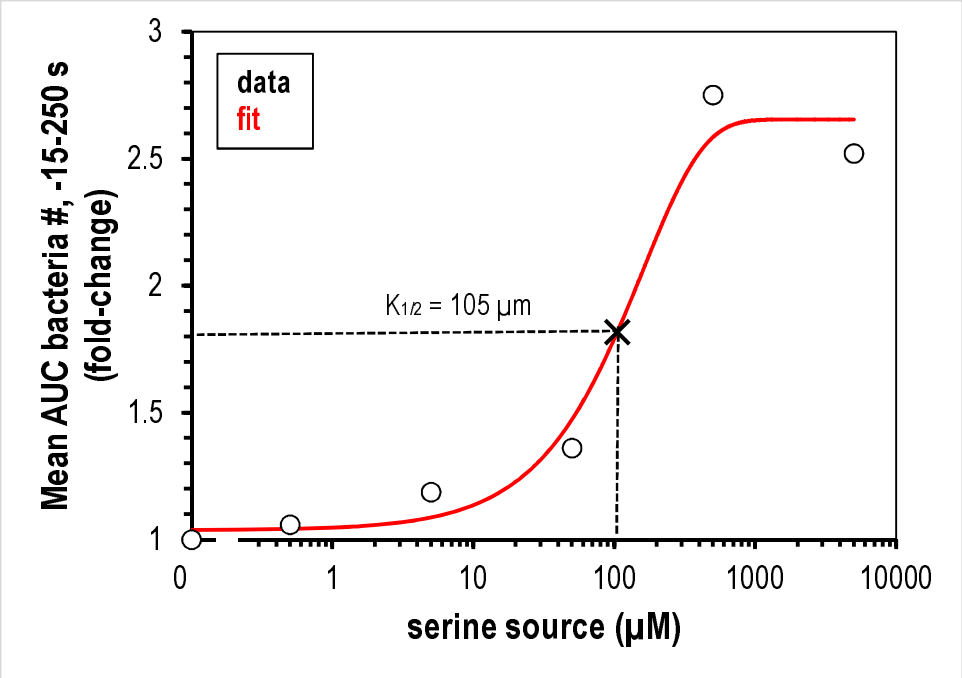

Fig. S3. Calculation of L-serine source required for half-maximal chemoattraction response ($K_{1/2}$). Data are mean AUC values of relative number of bacteria within 150 µm of the treatment location for the -15 s – 250 s range, represented as fold-change. Data are fit with an exponential curve (red line):

$$y = a + be^{-cx}$$

Where a=2.636193, b =-1.616338, and c=0.006282888. $K_{1/2}$ is approximated to be 105 µm (x, dashed lines).

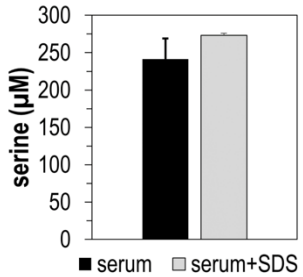

Fig. S4. Total serine present in human serum samples, as determined by mass spectrometry. Treatment with 50 µg recombinant serine dehydratase (SDS) over 4 h did not decrease L-serine content in human serum.

Supplemental Movies

Movie S1. Representative CIRA experiments with Alexa Fluor 488 dye (left) and *S. enterica* Typhimurium IR715 treated with human serum (right). Viewable at: https://www.youtube.com/watch?v=dyrQT2Ni5J8

Movie S2. Representative CIRA experiments comparing responses to human serum between *S. enterica* Typhimurium IR715 (*mplum*) and clinical isolates (*gfp*), as indicated. Viewable at: https://youtu.be/dwtZtoisjrU

Movie S3. Representative CIRA experiments comparing responses to human serum between WT *S. enterica* Typhimurium IR715 (*mplum* in left and center panel) and chemotactic mutants *tsr* (*gfp* in center panel, *mplum* in right panel), and *cheY* (*gfp* in left and right panel). Viewable at: https://youtu.be/O5zsEAqcJw8

Movie S4. Representative CIRA experiments comparing responses to 500 µM L-serine between *S. enterica* Typhimurium IR715 (*mplum*) and clinical isolates (*gfp*), as indicated. Viewable at: https://www.youtube.com/watch?v=p0Tsp06ZHO8

Movie S5. CIRA experiments comparing response of *S.* Typhimurium IR715 to L-serine or to norepinephrine. Cells are unprimed or primed with NE, as indicated. Viewable at: https://youtu.be/pUOlVjKYptc

Movie S6. CIRA experiments showing response of *S.* Typhimurium IR715 to DHMA. Cells are unprimed (left) or primed with NE (right). Viewable at: https://youtu.be/j4YL95QFCuI

Movie S7. Crystal structure of *S. enterica* Typhimurium Tsr LBD and comparison with *E. coli* Tsr LBD crystal structure (pdb: 3ATP). Viewable at: https://youtu.be/OlowDhRLNhA

Movie S8. Representative CIRA experiment showing response of *C. koseri* BAA-895 to human serum. Viewable at: https://youtu.be/9iMJz2OPbso

Movie S9. Representative CIRA experiment showing response of *E. coli* (pxS-gfp) MG1655 to human serum. Viewable at: https://www.youtube.com/watch?v=jq3cj9e52n4

Supplementary Tables

Table S1. Summary of crystallographic statistics

Protein, PDB code	*Se*Tsr LBD, PDB: 8FYV
Space Group	C 1 2 1
Cell dimensions and angle (a, b, c, beta) (Å, º)	125.8, 75.2, 129.6, 116.5
Resolution (Å) [a]	58.0-2.2 (2.26-2.20)
Completeness (%) [a]	100.0 (100.0)
Total reflections	1,039,561
Unique reflections	55,162
Average I/σ [a]	7.7 (3.6)
R_{merge} [a]	0.28 (1.42)
$CC_{1/2}$ [a]	0.994 (0.838)
R_{work} (%)	24.1
R_{free} (%)	25.8
Ramachandran favored, allowed, outliers (%)	99.1, 0.9, 0.0
Protein non-hydrogen atoms	5604

Solvent atoms	283
Protein chains, residues	5, 705
Average B-factor of protein atoms ($Å^2$)	49
Average B-factor of solvent atoms ($Å^2$)	43
rms bond lengths (Å)	0.002
rms bond angles (°)	0.42

[a] Values in parentheses indicate statistics for the highest resolution shell.

Supplementary data

Data S1. Database of Tsr homologue sequences.

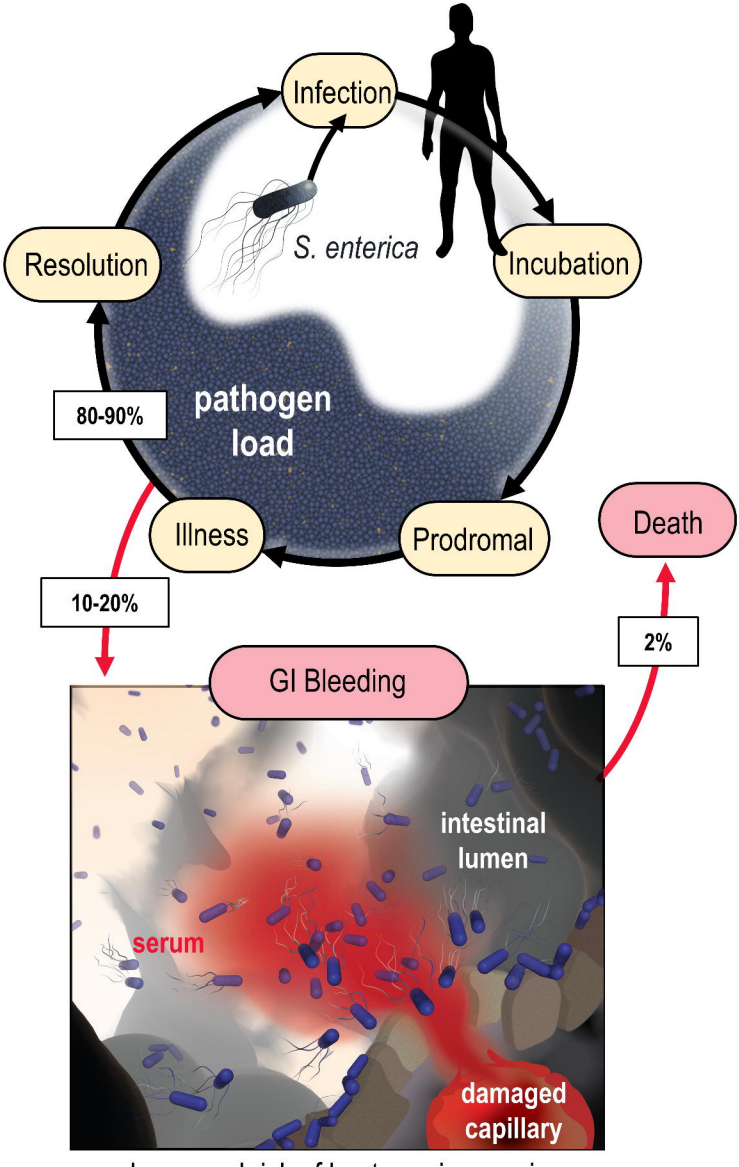
Infection
Incubation
Prodromal
Illness
Resolution
S. enterica
pathogen load
80-90%
10-20%
Death
2%
GI Bleeding
intestinal lumen
serum
damaged capillary
Increased risk of bacteremia, sepsis

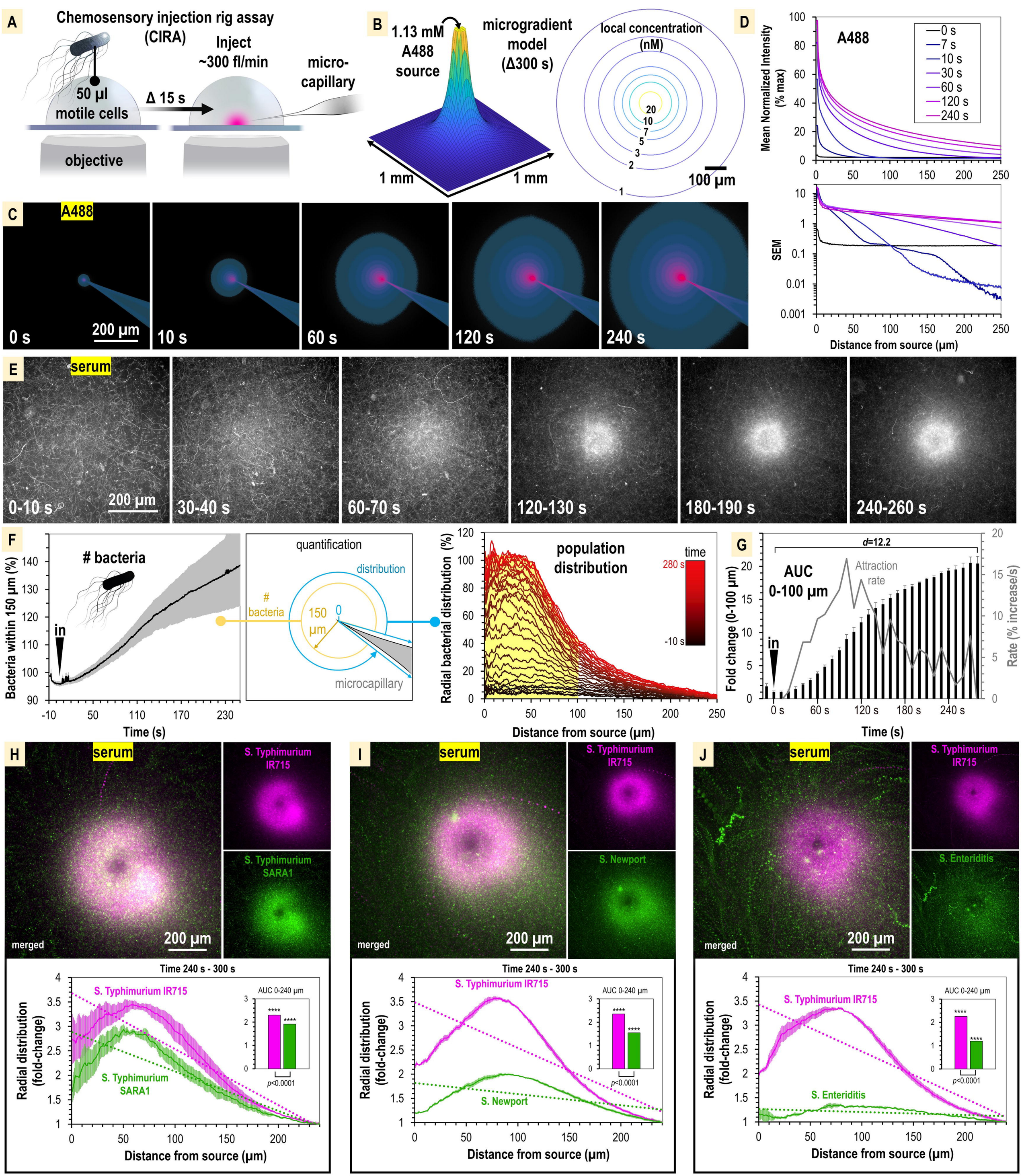
A
Chemosensory injection rig assay (CIRA)
Inject ~300 fl/min
micro-capillary
50 µl motile cells
Δ 15 s
objective
B
1.13 mM A488 source
microgradient model (Δ300 s)
local concentration (nM)
1 mm
1 mm
100 µm
C
A488
0 s
200 µm
10 s
60 s
120 s
240 s
D
A488
Mean Normalized Intensity (% max)
SEM
Distance from source (µm)
0 s
7 s
10 s
30 s
60 s
120 s
240 s
E
serum
0-10 s
200 µm
30-40 s
60-70 s
120-130 s
180-190 s
240-260 s
F
bacteria
Bacteria within 150 µm (%)
in
Time (s)
quantification
distribution
bacteria
150 µm
microcapillary
population distribution
time
280 s
-10 s
Radial bacterial distribution (%)
Distance from source (µm)
G
d=12.2
AUC 0-100 µm
Attraction rate
Fold change (0-100 µm)
Rate (% increase/s)
in
Time (s)
H
serum
S. Typhimurium IR715
S. Typhimurium SARA1
merged
200 µm
Time 240 s - 300 s
S. Typhimurium IR715
S. Typhimurium SARA1
AUC 0-240 µm
p<0.0001
Radial distribution (fold-change)
Distance from source (µm)
I
serum
S. Typhimurium IR715
S. Newport
merged
200 µm
Time 240 s - 300 s
S. Typhimurium IR715
S. Newport
AUC 0-240 µm
p<0.0001
Radial distribution (fold-change)
Distance from source (µm)
J
serum
S. Typhimurium IR715
S. Enteriditis
merged
200 µm
Time 240 s - 300 s
S. Typhimurium IR715
S. Enteriditis
AUC 0-240 µm
p<0.0001
Radial distribution (fold-change)
Distance from source (µm)

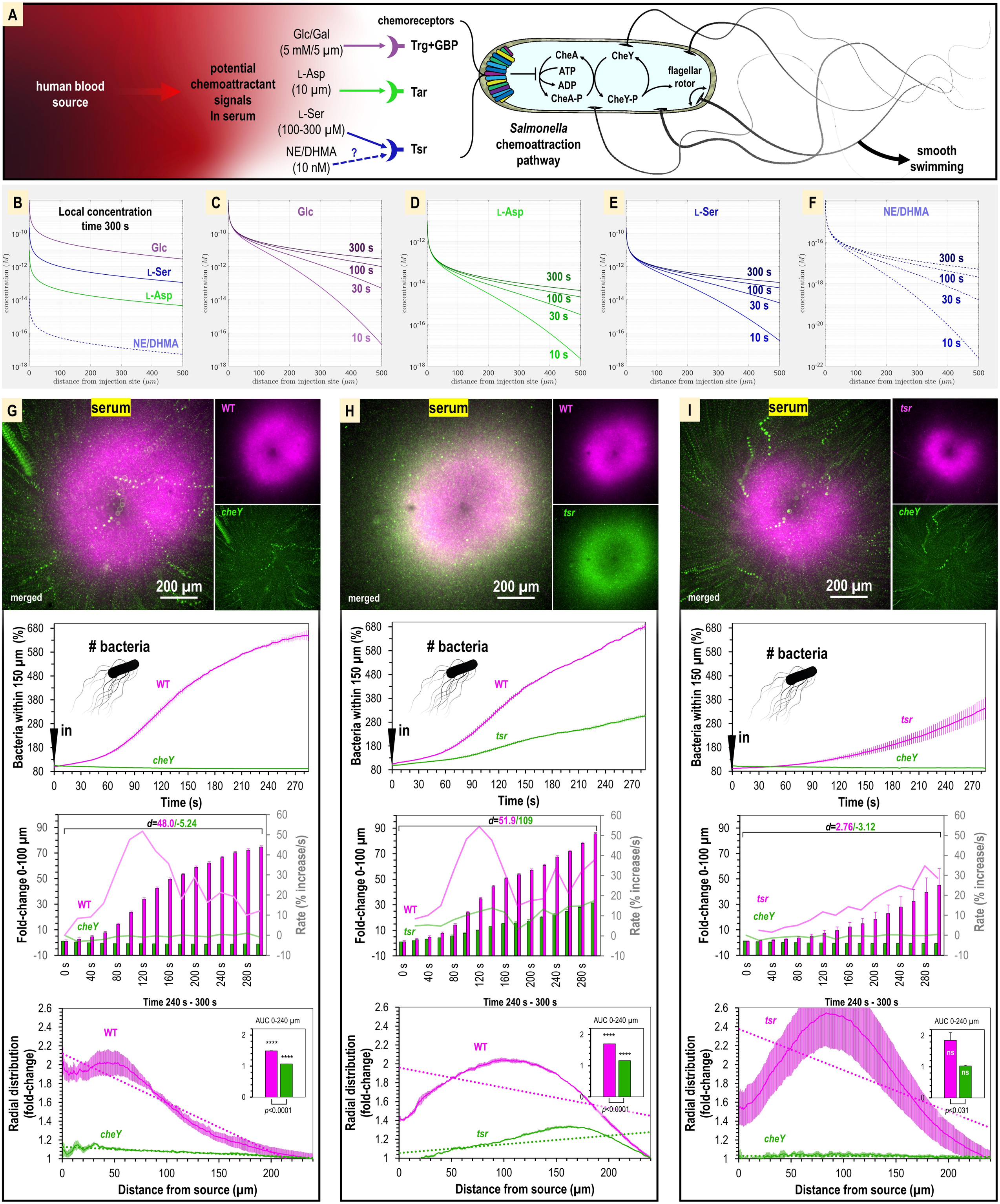
A
human blood source
potential chemoattractant signals In serum
Glc/Gal (5 mM/5 µm)
L-Asp (10 µm)
L-Ser (100-300 µM)
NE/DHMA (10 nM)
?
chemoreceptors
Trg+GBP
Tar
Tsr
CheA
ATP
ADP
CheA-P
CheY
CheY-P
flagellar rotor
Salmonella chemoattraction pathway
smooth swimming
B
Local concentration time 300 s
Glc
L-Ser
L-Asp
NE/DHMA
concentration (M)
distance from injection site (µm)
C
Glc
300 s
100 s
30 s
10 s
D
L-Asp
E
L-Ser
F
NE/DHMA
G
serum
WT
cheY
merged
200 µm
H
tsr
I
bacteria
in
Bacteria within 150 µm (%)
Time (s)
Fold-change 0-100 µm
Rate (% increase/s)
d=48.0/-5.24
d=51.9/109
d=2.76/-3.12
Time 240 s - 300 s
AUC 0-240 µm
p<0.0001
p<0.031
ns
Radial distribution (fold-change)
Distance from source (µm)

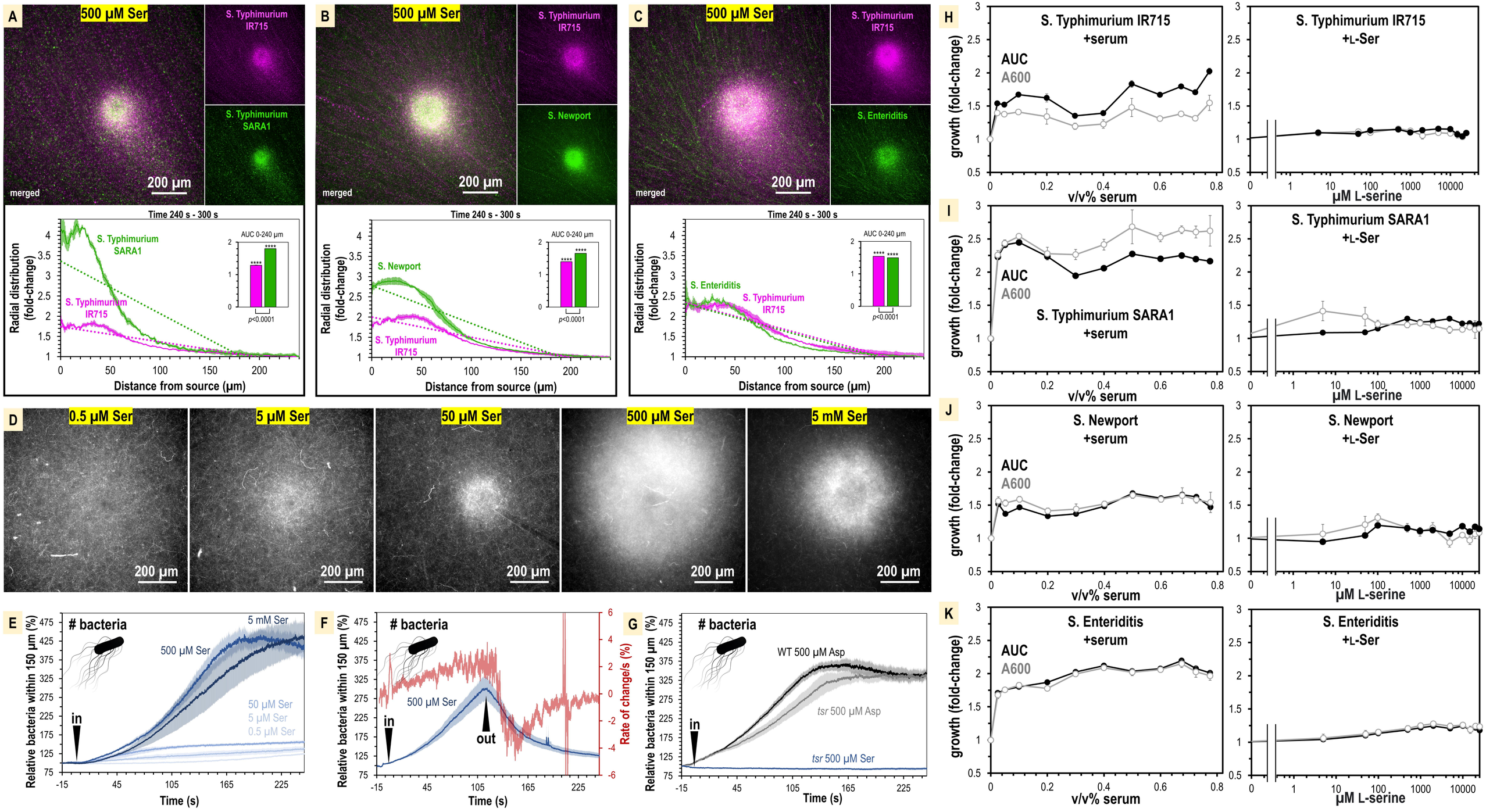
A
500 µM Ser
S. Typhimurium IR715
S. Typhimurium SARA1
merged
200 µm
Time 240 s - 300 s
Radial distribution (fold-change)
Distance from source (µm)
AUC 0-240 µm
p<0.0001
B
S. Newport
C
S. Enteriditis
D
0.5 µM Ser
5 µM Ser
50 µM Ser
500 µM Ser
5 mM Ser
E
bacteria
Relative bacteria within 150 µm (%)
Time (s)
in
F
out
Rate of change/s (%)
G
WT 500 µM Asp
tsr 500 µM Asp
tsr 500 µM Ser
H
S. Typhimurium IR715 +serum
S. Typhimurium IR715 +L-Ser
AUC
A600
growth (fold-change)
v/v% serum
µM L-serine
I
S. Typhimurium SARA1 +serum
S. Typhimurium SARA1 +L-Ser
J
S. Newport +serum
S. Newport +L-Ser
K
S. Enteriditis +serum
S. Enteriditis +L-Ser

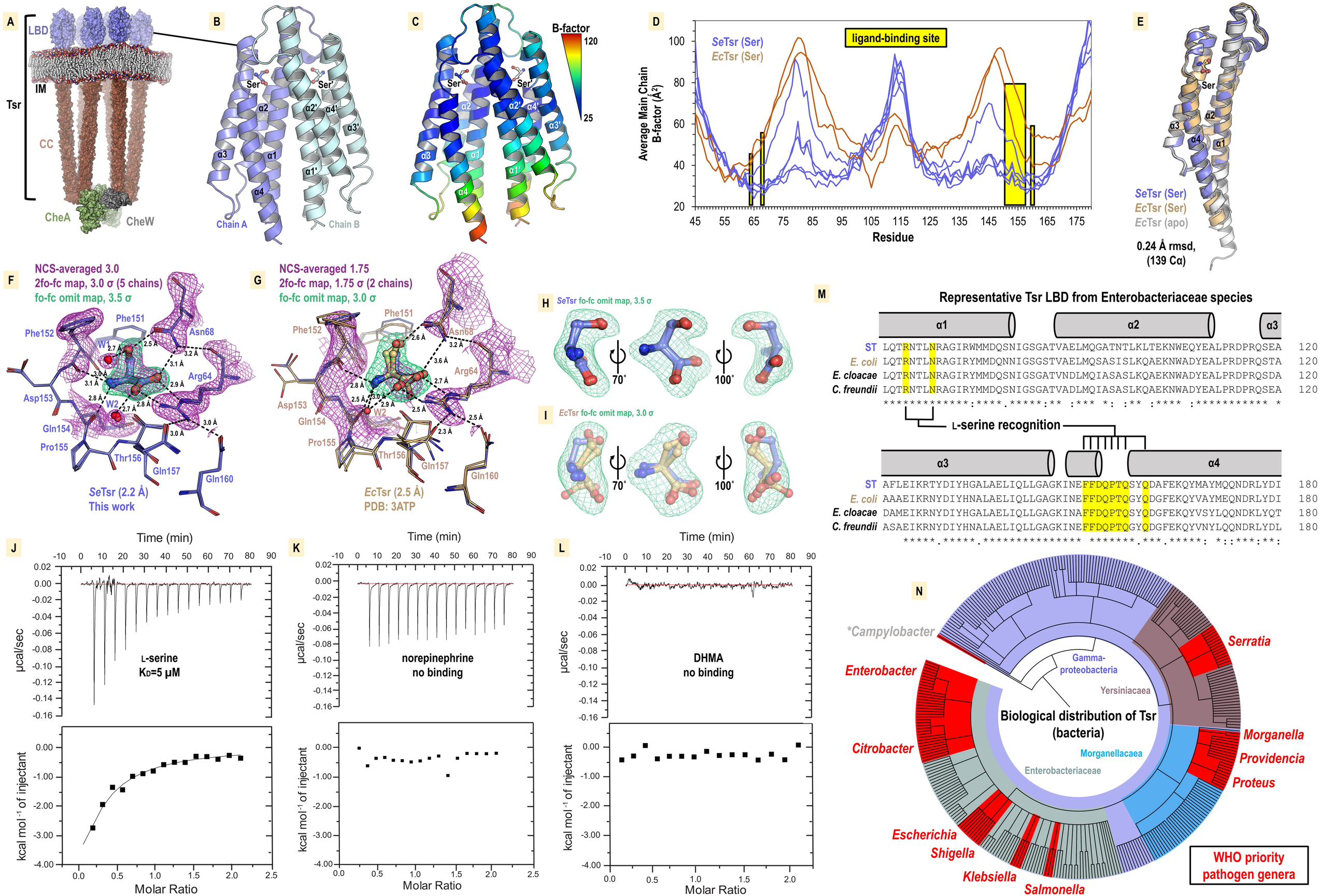
A
LBD
IM
Tsr
CC
CheA
CheW
B
Ser
Ser'
α2
α2'
α4'
α3'
α3
α1
α1'
α4
Chain A
Chain B
C
B-factor
120
25
D
SeTsr (Ser)
EcTsr (Ser)
ligand-binding site
Average Main Chain B-factor (Å²)
Residue
E
SeTsr (Ser)
EcTsr (Ser)
EcTsr (apo)
0.24 Å rmsd, (139 Cα)
F
NCS-averaged 3.0
2fo-fc map, 3.0 σ (5 chains)
fo-fc omit map, 3.5 σ
Phe151
Phe152
Asn68
Arg64
Asp153
Gln154
Pro155
Thr156
Gln157
Gln160
SeTsr (2.2 Å)
This work
G
NCS-averaged 1.75
2fo-fc map, 1.75 σ (2 chains)
fo-fc omit map, 3.0 σ
EcTsr (2.5 Å)
PDB: 3ATP
H
SeTsr fo-fc omit map, 3.5 σ
70˚
100˚
I
EcTsr fo-fc omit map, 3.0 σ
M
Representative Tsr LBD from Enterobacteriaceae species
α1
α2
α3
α4
ST LQTRNTLNRAGIRWMMDQSNIGSGATVAELMQGATNTLKLTEKNWEQYEALPRDPRQSEA 120
E. coli LQTRNTLNRAGIRYMMDQNNIGSGSTVAELMQSASISLKQAEKNWADYEALPRDPRQSTA 120
E. cloacae LQTRNTLNRAGIRYMMDQSNIGSGATVNDLMQIASASLKQAEKNWADYEALPRDPRQSDA 120
C. freundii LQTRNTLNRAGIRYMMDQSNIGSGATVADLMQIASASLKQAEKNWADYEALPRDPRQSEA 120
L-serine recognition
ST AFLEIKRTYDIYHGALAELIQLLGAGKINEFFDQPTQSYQDAFEKQYMAYMQQNDRLYDI 180
E. coli AAAEIKRNYDIYHNALAELIQLLGAGKINEFFDQPTQGYQDGFEKQYVAYMEQNDRLYDI 180
E. cloacae DAMEIKRNYDIYHGALAELIQLLGAGKINAFFDQPTQSYQDGFEKQYVSYLQQNDKLYQT 180
C. freundii ASAEIKRNYDIYHNALAELIQLLGAGKINEFFDQPTQGYQDGFEKQYVNYLQQNDRLYDL 180
J
Time (min)
μcal/sec
L-serine
KD=5 μM
kcal mol⁻¹ of injectant
Molar Ratio
K
norepinephrine
no binding
L
DHMA
no binding
N
*Campylobacter
Enterobacter
Citrobacter
Escherichia
Shigella
Klebsiella
Salmonella
Serratia
Morganella
Providencia
Proteus
Gamma-proteobacteria
Yersiniacaea
Morganellacaea
Enterobacteriaceae
Biological distribution of Tsr (bacteria)
WHO priority pathogen genera

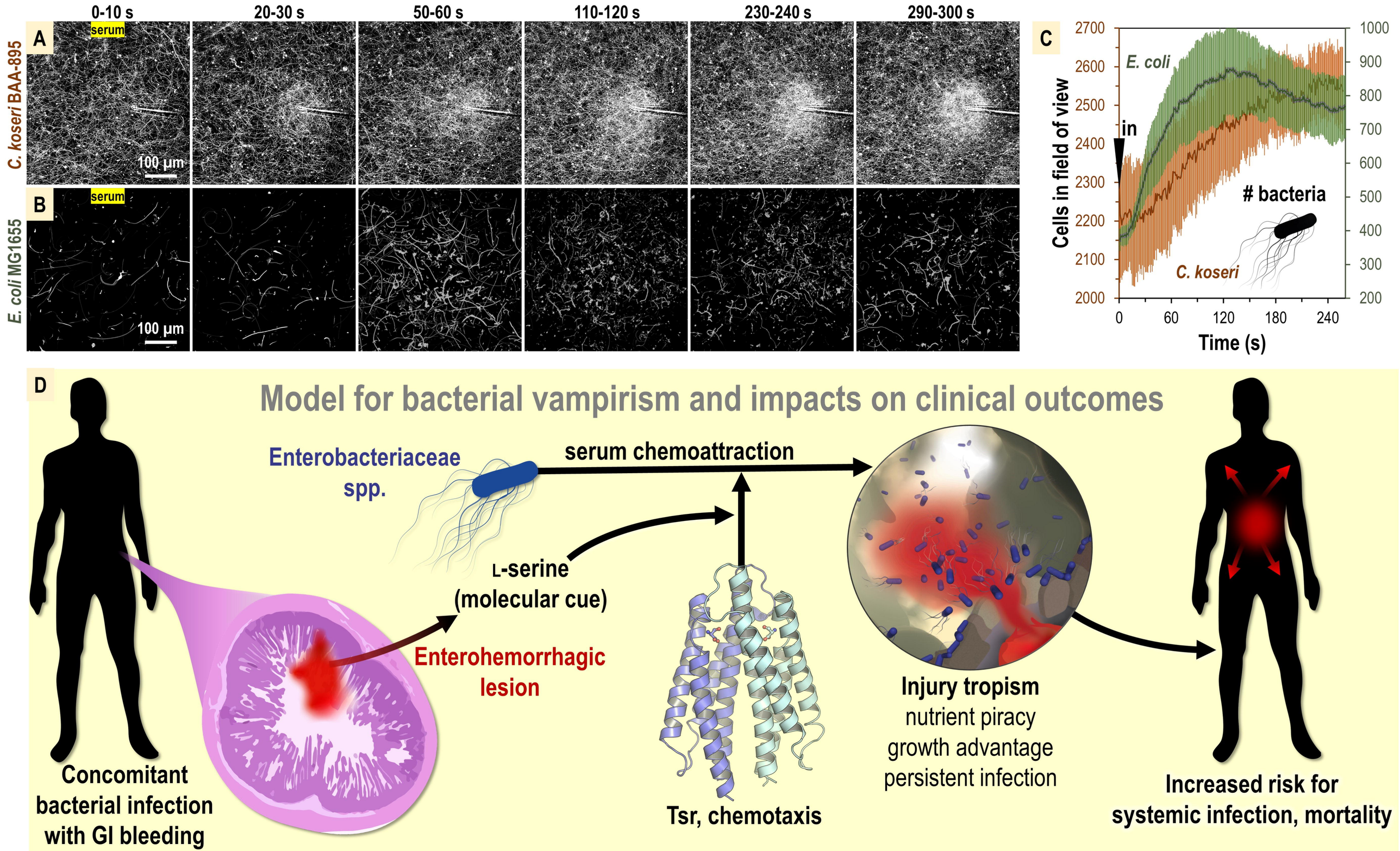
0-10 s
20-30 s
50-60 s
110-120 s
230-240 s
290-300 s
A
serum
C. koseri BAA-895
100 µm
B
serum
E. coli MG1655
100 µm
C
E. coli
in
bacteria
C. koseri
Cells in field of view
Time (s)
D
Model for bacterial vampirism and impacts on clinical outcomes
Enterobacteriaceae spp.
serum chemoattraction
L-serine (molecular cue)
Enterohemorrhagic lesion
Tsr, chemotaxis
Injury tropism
nutrient piracy
growth advantage
persistent infection
Concomitant bacterial infection with GI bleeding
Increased risk for systemic infection, mortality